

Lifetime measurements and shape coexistence in  $^{144}\text{Dy}$ 

M. G. Procter,<sup>1</sup> D. M. Cullen,<sup>1</sup> C. Scholey,<sup>2</sup> B. Niclasen,<sup>1</sup> P. J. R. Mason,<sup>1,\*</sup> S. V. Rigby,<sup>1,†</sup> J. A. Dare,<sup>1</sup> A. Dewald,<sup>3</sup> P. T. Greenlees,<sup>2</sup> H. Iwasaki,<sup>3</sup> U. Jakobsson,<sup>2</sup> P. M. Jones,<sup>2</sup> R. Julin,<sup>2</sup> S. Juutinen,<sup>2</sup> S. Ketelhut,<sup>2</sup> M. Leino,<sup>2</sup> N. M. Lumley,<sup>1</sup> O. Möller,<sup>4</sup> M. Nyman,<sup>2,‡</sup> P. Peura,<sup>3</sup> T. Pissulla,<sup>3</sup> A. Puurunen,<sup>2</sup> P. Rahkila,<sup>2</sup> W. Rother,<sup>3</sup> P. Ruotsalainen,<sup>2</sup> J. Sarén,<sup>2</sup> J. Sorri,<sup>2</sup> and J. Uusitalo<sup>2</sup>

<sup>1</sup>*Schuster Laboratory, University of Manchester, Manchester M13 9PL, United Kingdom*

<sup>2</sup>*Department of Physics, University of Jyväskylä, FIN-40014 Jyväskylä, Finland*

<sup>3</sup>*Institut für Kernphysik, Universität zu Köln, D-50937 Köln, Germany*

<sup>4</sup>*Institut für Kernphysik, Technische Universität Darmstadt, D-64289 Darmstadt, Germany*

(Received 10 March 2010; published 27 May 2010)

The known level scheme of  $^{144}\text{Dy}$  has been extended and lifetime measurements have been made with the recoil-distance Doppler-shift method. Reduced transition probabilities and deformations have been determined for four low-lying transitions. These states form part of the first observed band crossing, giving information on the change in nuclear deformation resulting from the rearrangement of  $h_{11/2}$  protons in the nucleus. Two bands built upon excited  $10^+$  states have been assigned  $\pi(h_{11/2})^2$  prolate and  $\nu(h_{11/2})^{-2}$  oblate configurations with  $\tau = 12(2)$  ps and  $0.01 < \tau \lesssim 16$  ns, respectively. These long lifetimes are reasoned to be a result of shape coexistence at low energy and moderate spin. A known four-quasiparticle dipole band has been extended to higher spin and lifetime measurements suggest a long-lived bandhead state. In this case, the excited states in the band may be consistent with a shears model interpretation of a magnetic dipole rotor. However, the measured  $B(M1)/B(E2)$  branching ratios reveal a larger than expected deformed rotational component compared with that in the analogous band in the lower mass isotope  $^{142}\text{Gd}$ .

DOI: [10.1103/PhysRevC.81.054320](https://doi.org/10.1103/PhysRevC.81.054320)

PACS number(s): 21.10.Tg, 23.20.Lv, 21.10.Ky, 27.60.+j

## I. INTRODUCTION

Neutron-deficient rare-earth nuclei in the mass  $A \approx 140$  region have been shown to exhibit a variety of structures as a result of their mid-shell occupancy of  $h_{11/2}$  intruder orbitals. Protons fill the lower part of the  $h_{11/2}$  shell with low- $\Omega$  orbitals favoring a prolate nuclear deformation, whereas for neutrons the Fermi surface lies around the high- $\Omega$   $h_{11/2}$  states, favoring an oblate deformation. The competition between these two high- $j$  intruder orbitals can result in ground-state deformations with a substantial degree of triaxiality for these  $\gamma$ -soft nuclei. Recent calculations by Möller and Bengtsson predict the ground state of  $^{144}\text{Dy}$  to contain a high degree of triaxiality with deformation parameters ( $\beta_2 = 0.20$ ,  $\beta_4 = 0.04$ ,  $\gamma = -25^\circ$ ) [1], which is interpreted within the framework of this high- $j$  orbital competition. The low-mass, even-even,  $N = 78$  isotones in this region—in particular  $^{142}\text{Gd}$  [2–7],  $^{140}\text{Sm}$  [8],  $^{138}\text{Nd}$  [9], and  $^{136}\text{Ce}$  [10]—have been the subject of much study. The systematic trends of these nuclei exhibit a variety of nuclear-structure effects, with the observation of isomeric states [5,10,11], magnetic rotation [2,12], and possible shape coexistence and triaxial rotation at moderate spins [5,7,9]. These features have all been described by the

differing overlap of wave functions as the various proton and neutron  $h_{11/2}$  orbitals are occupied. Detailed knowledge of the underlying single-particle configurations is, therefore, crucial for a complete understanding of the mechanisms giving rise to these effects. Recent work on  $^{144}\text{Dy}$  has established the presence of two bands built upon excited two-quasiparticle  $10^+$  states that decay directly into the ground-state band [12]. In addition, a dipole band was established at high spin and assumed to arise from the magnetic rotation of the nucleus, from a comparison with the well-known magnetic rotor  $^{110}\text{Cd}$  [12].

In this article, the results of an experiment performed at the University of Jyväskylä, Finland, are reported. The main aim of the experiment was the study of states above a weakly populated  $I^\pi = 8^-$  isomer in  $^{144}\text{Ho}$  [13,14]. The results presented here focus on the highly populated, two-proton exit channel,  $^{144}\text{Dy}$ , from the same fusion-evaporation reaction. The experiment was performed with the JUROGAM  $\gamma$ -ray spectrometer, coupled to the gas-filled recoil ion transport unit (RITU) and the GREAT focal-plane spectrometer [15–17]. This setup allowed the extension of the bands in  $^{144}\text{Dy}$  to higher spins, as well as the establishment of several new dipole bands. The experiment was performed in two parts: with and without the Köln differential plunger [18]. The plunger device was utilized at the JUROGAM target position, allowing the measurement of the lifetimes of several nuclear states. The distances selected in this work, for the study of  $^{144}\text{Ho}$ , limited the range of possible lifetime measurements to between 1 and 12 ps. These lifetimes were mainly suited for the measurement of the low-spin rotational states up to  $12\hbar$ . The results of these lifetime measurements point toward a possible shape coexistence in  $^{144}\text{Dy}$  at  $I^\pi = 10\hbar$  and shed some light on

\*Present address: Department of Physics, University of Surrey, Guildford, GU2 5XH, UK.

†Present address: Oliver Lodge Laboratory, University of Liverpool, Liverpool, L69 7ZE, UK.

‡Present address: Department of Physics, University of Helsinki, FIN-00014 Helsinki, Finland.

the previously identified, proposed magnetic rotational dipole band in Ref. [12].

## II. EXPERIMENTAL METHODS AND DATA ANALYSIS

### A. Spectroscopy

High-spin states were populated in  $^{144}\text{Dy}$  via the  $^{92}\text{Mo}(^{54}\text{Fe}, 2p)^{144}\text{Dy}$  reaction. A beam of  $^{54}\text{Fe}$  ions was accelerated by the K130 cyclotron at an energy of 226 MeV onto a  $550 \mu\text{g}/\text{cm}^2$   $^{92}\text{Mo}$  foil at the target position of the JUROGAM  $\gamma$ -ray spectrometer [19]. The beam current averaged  $\sim 12$  particle-nA (pNA) over an approximate running time of 46 h. In this reaction,  $^{144}\text{Dy}$  was populated with the largest relative cross section ( $\sim 60\%$ ), with the neighboring nuclei  $^{143}\text{Tb}$  ( $\sim 25\%$ ),  $^{143}\text{Dy}$  ( $\sim 5\%$ ), and  $^{140}\text{Gd}$  ( $< 5\%$ ) populated to a lesser extent. JUROGAM consisted of 43 Compton-suppressed HPGe detectors with a total photopeak efficiency of  $4.2 \pm 0.1\%$  at 1332 keV [20]. Fusion-evaporation products recoiled out of the target and passed through RITU [16,17], which separated the scattered beam from the recoils and transported the latter to the GREAT focal-plane spectrometer [15]. The flight time of the recoils through RITU in this mode was  $\sim 0.5 \mu\text{s}$ . The standard GREAT configuration [15] comprised a multiwire proportional counter (MWPC) at the entrance to two double-sided silicon strip detectors (DSSD) [20] into which the recoiling nuclei were implanted.

### B. Lifetimes

For the study of lifetime data using the recoil distance Doppler shift (RDDS) technique, the target mount was replaced with the Köln differential-plunger device [18]. This setup restricted the number of JUROGAM detectors that could be used to those at backward angles of  $158^\circ$ ,  $134^\circ$ , and  $108^\circ$ , reducing the total photopeak efficiency of the array to  $\sim 2\%$ . The same reaction was utilized at a beam energy of 226 MeV and an average beam intensity of  $\sim 2$  pNA for 115 h. The reduced beam intensity was necessary because of the extra  $\gamma$ -ray scattering, which occurred from the addition of the plunger device around the target. The plunger device housed both the  $^{92}\text{Mo}$  target and a  $1 \text{ mg}/\text{cm}^2$  Mg degrader foil to reduce the full recoil velocity from  $v/c = 0.032(2)$  to  $v/c = 0.020(5)$ . Scattering of recoils in the Mg degrader foil reduced the transmission efficiency of RITU by  $\sim 1/3$ . In this report, fully Doppler shifted and degraded  $\gamma$  rays are defined as those detected prior to and after transmission through the degrader foil, respectively. This distinction is necessary when dealing with the calculation of state lifetimes. Measurements were made with target-to-degrader distances of 6.4(1), 8.5(2), 12.4(1), 22.9(2), 31.8(2), 42.3(2), 68.7(6), and 105.9(10)  $\mu\text{m}$ . The degraded fusion-evaporation recoils passed through RITU where they were transported to the GREAT focal-plane spectrometer [15]. The flight time of the degraded recoils through RITU was  $\sim 0.8 \mu\text{s}$ .

### C. Data analysis

In each part of the experiment, events were time-stamped by a 100-Mhz clock, through the triggerless total data readout (TDR) acquisition system [21]. Conditions were imposed

on the time of flight (ToF) of the recoils from the target position to the focal plane, so that decays in JUROGAM could be correlated later in software, with signals detected in the DSSD, to form events. In conjunction with this, the MWPC time stamp provided a method for discerning beamlike and targetlike nuclei, helping reduce the number of uncorrelated background signals detected at the target position. Data were collected for off-line sorting with the GRAIN software package [22]. The data were sorted into two-dimensional asymmetric spectra (matrices) and symmetric three-dimensional spectra (cubes) for analysis with the UPAK [23] and RADWARE [24] software suites, respectively. Directional correlation from oriented states (DCO) ratios were calculated by sorting data from the ten detectors in Ring 2 of the JUROGAM array at a backward angle of  $134^\circ$ , with the ten detectors in the combined Rings 4 and 5 at angles  $94^\circ$  and  $86^\circ$ , respectively. After setting gates in rings at  $134^\circ$  and  $90^\circ$ , the intensities of the transitions of interest were measured to be  $I_\gamma(90^\circ)$  and  $I_\gamma(134^\circ)$ , respectively, and the DCO ratio is calculated as

$$R_{\text{DCO}} = \frac{I_\gamma(90^\circ)}{I_\gamma(134^\circ)}. \quad (1)$$

Gates were summed across a set of strong quadrupole transitions on both axes to allow the calculation of the lowest intensity transitions.

The lifetime data were analyzed using the differential decay curve method (DDCM), a well-established technique for calculating excited state lifetimes from RDDS experiments [25,26]. The lifetime of an excited nuclear state, as measured for a specific target-to-degrader distance,  $x$ , is calculated [26,27] from

$$\tau(x) = \frac{\{C_s, A_d\} - \alpha\{C_s, B_d\}}{\frac{d}{dx}\{C_s, A_s\}} \frac{1}{\langle v \rangle}, \quad (2)$$

where  $\langle v \rangle$  is the mean velocity of the fusion-evaporation recoils. The quantities  $A$ ,  $B$ , and  $C$  refer to the intensities of the fully Doppler shifted ( $s$ ) and degraded ( $d$ ) components of the measured photopeaks, where the  $\gamma$  ray depopulating the level of interest,  $A$ , is fed by the  $\gamma$  ray  $B$ , with a coincidence gate set on a higher lying transition,  $C$ . The terms  $\{C_s, A_s\}$ , for example, refer to the normalized intensity of the shifted component of the transition  $A$  after a gate has been set on the shifted component of transition  $C$ . The transition intensities were normalized to the total number of counts in both the Doppler-shifted and degraded peaks to account for the difference in experimental data collection periods for each distance. In the coincidence method, gates are set above the level of interest, and consequently, the effects of unknown side feeding are removed. In this case the value of  $\alpha$  accounts for any additional unobserved decays that could depopulate the state of interest. Intensity considerations gave a limit on the maximum possible effect that any unobserved transitions could introduce in the measured lifetime. In this work, it was deduced that the lifetimes were unaffected by a variation of  $\alpha$  within the maximum intensities established from the analysis of the  $\gamma$ - $\gamma$  data, and, consequently,  $\alpha$  was taken to be one.

In this work, the geometry of the JUROGAM detector array necessitated gating on detectors at  $108^\circ$  to the beam line, where the fully Doppler shifted and degraded components of a  $\gamma$ -ray

transition are not well separated. In this case, gates were placed across the full widths of the transitions  $C$ . This introduces an additional element of background into the observed intensities of both the feeding and depopulating transitions, which is accounted for by including the intensities of both of these transitions in the analysis [28], as in Eq. (2).

With this approach, measurements were made by summing the gates on the indirect-feeding transitions. These gates were set on detectors in Ring 3 of the JUROGAM array, in the matrix consisting of transitions in Ring 2 versus Ring 3. The areas of the direct feeding and depopulating components at each target-to-degrader distance were determined from the projected spectrum corresponding to detectors in Ring 2, at a backward angle of  $134^\circ$  to the beam line. Lifetime values were then determined by simultaneously fitting piecewise the normalized decay curve of the level of interest, and the derivative of this function, with a number of second-order polynomials. This resulted in a set of “distance-independent”  $\tau(x)$  values, where any deviation from a straight line was used to reveal any possible systematic errors in the analysis.

### III. RESULTS

#### A. Level scheme of $^{144}\text{Dy}$

The  $^{144}\text{Dy}$  level scheme resulting from the present work is shown in Fig. 1. The level scheme has been considerably extended in excitation energy and spin from previous studies [12,29], with the identification of four new dipole bands DB1, DB2, DB4, and DB5. It should be noted that the level scheme presented in this work has been reorganized with reference to the most recent work on  $^{144}\text{Dy}$  [12]. This reordering better demonstrates the similarities between the excited states in  $^{144}\text{Dy}$  and the lower mass even-even isotones (see Sec. IV A2) and the trends in lifetimes of these states (see Sec. IV B). Table I contains the spectroscopic information for all of the  $\gamma$  rays established in this work.

Spin assignments were made using DCO ratios. As an internal calibration, DCO ratios were made for several stretched quadrupole and stretched dipole transitions established in previous works [12,29]. The values measured in this work for the four lowest lying, well-known quadrupole transitions in the ground-state band of  $^{144}\text{Dy}$  revealed a weighted average value of  $R_{\text{DCO}} = 0.90(1)$ . The weighted average of the 859- and 427-keV transitions, established to be dipoles in Ref. [12], in this work have a value of  $R_{\text{DCO}} = 0.66(5)$ . In comparison, the experimental DCO ratios for all of the measured transitions in this work, with the exception of DB3 (see later), gave weighted average values of  $R_{\text{DCO}} = 0.90(1)$  and  $R_{\text{DCO}} = 0.59(1)$  for quadrupole and dipole transitions, respectively.

##### 1. Band 1

Figure 2(a) shows the result of a double gate set on the 610- and 665-keV transitions in Band 1, from which the higher lying transitions (761, 772, and 827 keV) can be seen. Band 1 has been extended with the addition of the 827-keV transition, and the 461-keV transition is now established to feed in from

DB1 to Band 1, rather than a continuation of the band as was assigned to Band f in Ref. [12]. The 708-keV transition, previously placed lower in the band and parallel to all other transitions in Ref. [12], is established in the present work to decay from the  $22^+$  level in DB1. Figure 2(b) shows the spectrum resulting from a double gate set on the 772- and 761-keV transitions in Band 1. The presence of the 708-keV transition, with possibly a larger intensity than in Fig. 2(a), confirms its new placement above the gates set in the band. The 506- and 717-keV transitions, previously placed in this band, but parallel to the 772-keV transition in Ref. [12], are also present in Fig. 2(b), suggesting that they feed directly into the band. The DCO ratios for the 506- and 717-keV  $\gamma$  rays have dipole character, and, coupled with their presence in the sum of triple-gated spectra for all transitions in Band 3, [see Fig. 2(e)], both transitions have been tentatively assigned to DB5. The  $363 \rightarrow 250$  keV transitions in DB1 are also visible in Fig. 2(a) at low intensity because they are established to link into Band 1 by the 461- and 871-keV transitions. These are evident in Fig. 3 in Ref. [12]; however, they were not discussed, presumably because of their low intensity and lack of statistics. The presence of the 355-keV transition in Fig. 2(a) suggests that Band 1 is also fed from the lower levels in DB2; however, the linking transitions could not be identified in this work. The measured DCO ratios confirm the quadrupole nature of the in-band transitions ( $610 \rightarrow 761$  keV) above the  $8^+$  state.

##### 2. Band 2

Figure 2(c) shows a double gate on the 798- and 848-keV transitions in Band 2. This band has been extended with the addition of four  $\gamma$ -ray transitions (855, 914, 1008, and 1121 keV), with DCO ratios confirming the quadrupole nature of decays from the  $16^+$ ,  $18^+$ , and  $20^+$  excited states (see Table I). Figure 2(d) shows a sum of triple gates of all transitions below the excited  $16^+$  state in Band 2 ( $552 \rightarrow 798$  keV) and the ground-state sequence in Band 1 ( $493 \rightarrow 649$  keV). This spectrum reveals the newly established linking transitions from DB1 (1061 keV) and DB2 (1236 keV) as well as the 1082-keV transition that feeds into the  $16^+$  state.

##### 3. Band 3

Figure 2(e) shows a sum of double gates of all transitions in Band 3. The only other band observed to feed into Band 3 is DB5 ( $506 \rightarrow 617$  keV), which is placed tentatively at higher spin. This placement also accounts for the presence of transitions from DB5 established in the spectrum gated on the 422-keV transition in DB1 [see Fig. 4(a)]. The 506-keV transition, previously assigned to Band 3 (Band a) in Ref. [12], is now placed in DB5, and a new intense 684-keV transition is placed in the band. In this work the 528- and 570-keV transitions have their ordering reversed from that in the previous work [12]. This is based upon lifetime considerations and comparisons with neighboring nuclei discussed in Section IV A2. The 570-keV transition also appears to be a doublet, with a component present in DB5. The large intensity of transitions in the ground-state band



TABLE I.  $\gamma$ -ray energies, intensities, spin assignments, and DCO ratios for the transitions in  $^{144}\text{Dy}$ .

$E_\gamma$ (keV)	$I_\gamma$	$R_{\text{DCO}}$	$\sigma L$	$J_i^\pi \rightarrow J_f^\pi$	Band
87.9(1)	2.0(1)	–	$M1$	$13^- \rightarrow 12^-$	$4 \rightarrow 12^-$
152.6(4)	5.1(2)	0.46(10)	$M1$	$16^- \rightarrow 15^-$	DB3
169.0(1)	11.4(4)	1.07(11)	$M1/E2$	$16^- \rightarrow 15^-$	DB3
184.2(1)	1.1(1)	–	$(M1)$	$12^+ \rightarrow 12^+$	$1 \rightarrow 2$
190.4(1)	1.1(1)	–	$(M1)$	$16^+ \rightarrow 16^+$	$1 \rightarrow 2$
206.3(1)	14.6(5)	–	$M1$	$19^- \rightarrow 18^-$	DB3
207.6(1)	22.1(8)	0.96(2)	$M1/E2$	$18^- \rightarrow 17^-$	DB3
227.8(1)	1.0(10)	–	$(M1)$	$14^+ \rightarrow 14^+$	$1 \rightarrow 2$
242.3(1)	0.9(1)	–	$(M1)$	$20^+ \rightarrow (19^+)$	DB1 $\rightarrow$ DB2
249.8(1)	1.2(1)	0.60(7)	$M1$	$22^+ \rightarrow 21^+$	DB1
267.4(1)	24.3(8)	0.97(5)	$M1/E2$	$17^- \rightarrow 16^-$	DB3
269.8(5)	0.3(1)	–	$(M1)$	$18^+ \rightarrow (17^+)$	DB1 $\rightarrow$ DB2
279.1(1)	1.7(1)	–	$(M1)$	$19^+ \rightarrow (18^+)$	DB1 $\rightarrow$ DB2
319.8(1)	14.8(5)	0.92(6)	$E2$	$7^- \rightarrow 5^-$	4
327.2(1)	3.0(1)	–	$(M1)$	$(25^-) \rightarrow (24^-)$	DB4
351.0(1)	1.3(1)	–	$(M1)$	$(28^-) \rightarrow (27^-)$	DB4
352.8(1)	3.9(2)	–	$(M1)$	$(18^+) \rightarrow 17^+$	DB2
355.4(1)	4.4(2)	–	$(M1)$	$(17^+) \rightarrow 16^+$	DB2
362.7(1)	3.2(2)	0.52(3)	$M1$	$19^+ \rightarrow 18^+$	DB1
381.3(1)	14.4(5)	1.19(6)	$M1/E2$	$20^- \rightarrow 19^-$	DB3
383.2(1)	3.4(3)	–	$(M1)$	$(24^-) \rightarrow (23^-)$	DB3
387.8(1)	2.1(1)	–	$(M1)$	$(26^-) \rightarrow (25^-)$	DB5
390.6(1)	3.0(1)	–	$(M1)$	$(26^-) \rightarrow (25^-)$	DB4
400.4(1)	5.2(2)	–	$(M1)$	$22^- \rightarrow 21^-$	DB3
403.2(1)	3.8(2)	0.66(4)	$M1$	$21^+ \rightarrow 20^+$	DB1
417.6(1)	2.8(1)	1.04(18)	$E2$	$9^- \rightarrow 7^-$	$4 \rightarrow 7^-$
422.3(1)	5.7(2)	0.45(6)	$M1$	$20^+ \rightarrow 19^+$	DB1
426.8(1)	11.2(5)	0.60(7)	$E1$	$7^- \rightarrow 6^+$	4
436.9(1)	2.1(1)	0.58(2)	$M1$	$16^+ \rightarrow 16^+$	DB2 $\rightarrow$ 2
454.6(1)	4.0(3)	–	$(M1)$	$(24^-) \rightarrow (23^-)$	DB4
456.4(2)	1.1(2)	–	$(M1)$	$(29^-) \rightarrow (30^-)$	DB4
459.0(1)	2.2(2)	–	$(M1)$	$(19^+) \rightarrow 18^+$	DB2
460.9(1)	7.0(3)	1.02(30)	$E2/M1$	$19^+ \rightarrow (18^+)$	DB1 $\rightarrow$ 1
466.6(1)	1.5(1)	–	$(M1)$	$(27^-) \rightarrow (26^-)$	DB4
482.1(1)	3.7(4)	0.90(6)	$E2$	$7^- \rightarrow 5^-$	$7^- \rightarrow 4$
492.7(1)	100.0(40)	0.94(2)	$E2$	$2^+ \rightarrow 0^+$	1
502.8(1)	15.1(5)	0.71(3)	$M1/E2$	$21^- \rightarrow 20^-$	DB3
506.0(1)	6.2(3)	0.52(3)	$M1$	$(23^-) \rightarrow (22^-)$	DB5
513.7(1)	3.9(2)	–	$(M1)$	$(25^-) \rightarrow 24^-$	DB3
528.4(1)	7.5(6)	0.81(6)	$E2$	$10^+ \rightarrow 8^+$	3
538.9(1)	23.7(9)	0.83(4)	$E2$	$12^+ \rightarrow 10^+$	2
551.5(1)	25.8(10)	0.86(4)	$E2$	$10^+ \rightarrow 8^+$	2
570.1(1) <sup>a</sup>	7.4(4)	0.87(3)	$E2$	$12^+ \rightarrow 10^+$	3
570.0(1) <sup>a</sup>	3.8(2)	–	$(M1)$	$(25^-) \rightarrow (24^-)$	DB5
579.1(1)	17.3(7)	1.18(11)	$E2$	$9^- \rightarrow 7^-$	4
588.0(1)	9.8(4)	1.01(12)	$E2$	$20^- \rightarrow 18^-$	DB3
589.6(1)	1.9(3)	–	$E1$	$7^- \rightarrow 6^+$	$7^- \rightarrow 1$
593.1(2)	2.1(2)	–	$(M1)$	$(23^-) \rightarrow 22^-$	DB3
609.8(1)	19.7(9)	0.92(5)	$E2$	$10^+ \rightarrow 8^+$	1
617.0(1)	1.8(2)	0.56(3)	$M1$	$(27^-) \rightarrow (26^-)$	DB5
625.2(1)	6.4(7)	0.77(12)	$M1$	$12^- \rightarrow 11^-$	$12^- \rightarrow 4$
649.1(1)	58.2(20)	0.86(3)	$E2$	$8^+ \rightarrow 6^+$	1
664.8(1)	19.2(7)	1.13(8)	$E2$	$12^+ \rightarrow 10^+$	1
672.3(1)	99.0(40)	0.89(2)	$E2$	$4^+ \rightarrow 2^+$	1
680.4(1)	21.7(8)	0.82(16)	$E2$	$14^+ \rightarrow 12^+$	2
684.2(1)	3.8(2)	0.96(21)	$E2$	$18^+ \rightarrow 16^+$	3
688.0(1)	6.1(4)	0.51(12)	$M1$	$8^- \rightarrow 7^-$	$8^- \rightarrow 4$

TABLE I. (*Continued.*)

$E_\gamma$ (keV)	$I_\gamma$	$R_{\text{DCO}}$	$\sigma L$	$J_i^\pi \rightarrow J_f^\pi$	Band
708.4(1)	2.3(2)	–	(E2)	$22^+ \rightarrow (20^+)$	DB1 $\rightarrow$ 1
713.1(1)	11.8(5)	0.99(25)	E2	$13^- \rightarrow 11^-$	4
717.0(1)	6.1(3)	0.68(2)	M1	$(24^-) \rightarrow (23^-)$	DB5
724.5(1)	18.5(7)	0.90(8)	E2	$14^+ \rightarrow 12^+$	1
738.3(1)	9.8(4)	0.85(9)	E2	$15^- \rightarrow 13^-$	4
751.0(1)	74.0(30)	0.85(3)	E2	$6^+ \rightarrow 4^+$	1
754.6(1)	7.5(5)	–	E2	$15^- \rightarrow 13^-$	DB3 $\rightarrow$ 4
760.9(1)	15.9(6)	1.05(7)	E2	$16^+ \rightarrow 14^+$	1
762.5(1)	19.8(8)	0.89(7)	E2	$11^- \rightarrow 9^-$	4
772.2(1)	11.3(5)	–	(E2)	$(18^+) \rightarrow 16^+$	1
781.4(2)	3.7(2)	0.83(10)	E2	$20^+ \rightarrow 18^+$	3
798.4(1)	14.5(5)	0.99(8)	E2	$16^+ \rightarrow 14^+$	2
801.8(1)	4.0(2)	–	E1	$15^- \rightarrow 14^+$	4 $\rightarrow$ 2
827.1(2)	3.4(3)	–	(E2)	$(20^+) \rightarrow (18^+)$	1
831.0(1)	3.3(3)	–	(E2)	$(10^-) \rightarrow 8^-$	[(10 <sup>-</sup> ) $\rightarrow$ 8 <sup>-</sup> ]
848.3(1)	6.4(3)	1.04(8)	E2	$18^+ \rightarrow 16^+$	2
854.5(1)	3.5(3)	0.81(8)	E2	$20^+ \rightarrow 18^+$	2
858.8(1)	22.0(13)	0.66(5)	E1	$5^- \rightarrow 4^+$	4
870.7(2)	2.1(2)	0.99(12)	E2	$18^+ \rightarrow 16^+$	DB1 $\rightarrow$ 1
903.3(1)	9.7(4)	0.85(11)	E2	$22^- \rightarrow 20^-$	DB3
914.0(2)	2.2(2)	–	(E2)	$(22^+) \rightarrow 20^+$	2
976.8(1)	7.2(3)	–	(E2)	$(24^-) \rightarrow 22^-$	DB3
986.3(1)	5.3(3)	0.95(7)	E2	$14^+ \rightarrow 12^+$	3
994.0(1)	1.6(2)	–	(E2)	$(23^-) \rightarrow 21^-$	DB3
1008.2(3)	1.2(2)	–	(E2)	$(24^+) \rightarrow (22^+)$	2
1013.7(1)	3.8(3)	0.97(9)	E2	$16^+ \rightarrow 14^+$	3
1061.3(1)	3.4(2)	1.04(5)	E2	$18^+ \rightarrow 16^+$	DB1 $\rightarrow$ 2
1082.3(3)	1.8(2)	–	(E2)	$(18^+) \rightarrow 16^+$	$(18^+) \rightarrow$ 2
1121.3(3)	1.0(1)	–	(E2)	$(26^+) \rightarrow (24^+)$	2
1235.8(1)	3.0(2)	1.00(8)	E2	$16^+ \rightarrow 14^+$	DB2 $\rightarrow$ 2

<sup>a</sup>570-keV  $\gamma$  ray is a doublet with components in Band 3 and DB5.

quadrupole character, assumed to be E2, in stark contrast to previous measurements, which assign it an M1 character [12]. However, the E2 assignment of the new 418- and 482-keV transitions from the DCO measurements are consistent with the quadrupole assignment for the 579-keV transition made here (see Table I).

### 5. DB1 and DB2

Figure 4(a) shows a spectrum resulting from a single gate on the 422-keV transition in DB1. This spectrum clearly shows the transitions linking both DB1 and DB2 to bands 1 and 2, as well as the 461-keV  $\gamma$  ray that depopulates the  $19^+$  excited state in DB1. DCO ratios for the 1061- and 871-keV transitions confirm the  $I^\pi = 18^+$  spin assignment to the bandhead of DB1. The positive parity assigned to DB1 arises from the assignments made to similar bands observed in  $^{142}\text{Gd}$  [4]. The four transitions above this level all have dipole character, suggesting that the 461-keV transition feeding the  $18^+$  state in Band 1 is also of a dipole nature. The DCO ratio for this transition was measured to be 1.02(30) (see Table I), which, because of its large uncertainty, is consistent with either a quadrupole or dipole nature. Higher statistics are required to better measure the DCO ratio for the 461-keV transition, and

to fully establish its multipolarity. DCO ratios for the 1236- and 437-keV transitions depopulating the bandhead state in DB2 confirm its spin assignment as  $16^+$ , with the positive parity assigned as in DB1. A lack of statistics prevented the measurement of DCO ratios for the transitions above this level in DB2; however, comparisons with the other dipole bands observed in  $^{144}\text{Dy}$  in this work suggest a dipole character for all three transitions (355, 353, and 459 keV).

The spectrum in Fig. 4(a) also confirms the placement of DB5 at high spin because states assigned to this band can be seen in this spectrum gated on the 422-keV transition in DB1. However, the lack of observation of the 506-keV transition implies that the higher lying DB5 must decay into DB1 below the  $20^+$  excited level. The presence of all of the other transitions assigned to DB5 suggests that it does feed into the higher spin states of DB1 around  $\sim 22^+$ , from a level above the bandhead state.

### 6. DB5

Figure 4(b) shows a double-gated spectrum on the 506- and 570-keV transitions in DB5. The spectrum shows that the 570-keV transition is a doublet with the second component established to lie in Band 3. All other transitions assigned

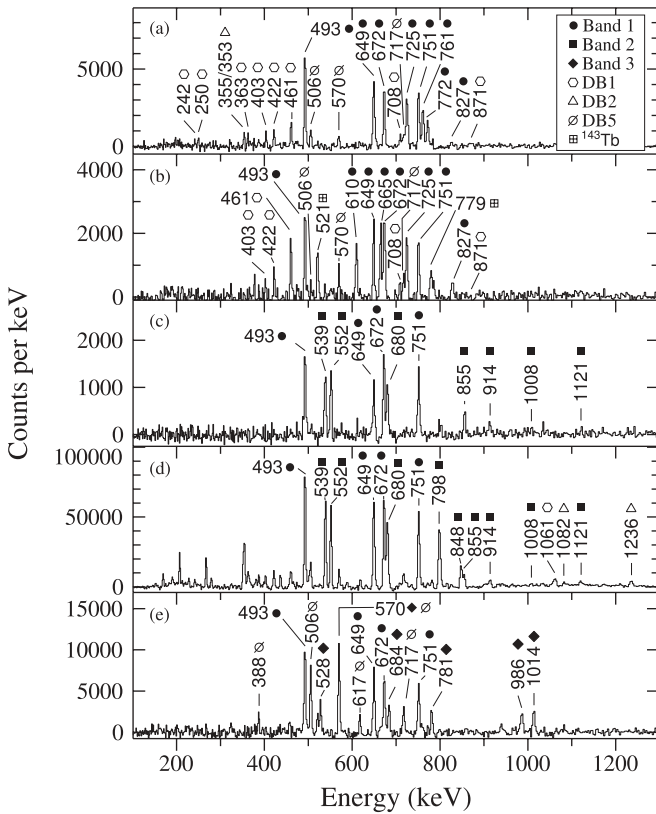


FIG. 2. Background-subtracted double-gated coincidence spectra of  $^{144}\text{Dy}$  recorded with the JURIGAM array. Only the most prominent  $\gamma$  rays are indicated. Spectrum (a) corresponds to a double gate on the 665- and 610-keV transitions in Band 1, and spectrum (b) to a double gate on the 761- and 772-keV transitions in Band 1. Spectrum (c) is a double gate on the 798- and 848-keV transitions in Band 2 and spectrum (d) is a sum of all triple gates of transitions below the  $16^+$  state in Band 2 ( $493 \rightarrow 798$  keV). Spectrum (e) is the sum of all double gates of transitions in Band 3 ( $528 \rightarrow 781$  keV).

to Band 3 are evident in this spectrum. The presence of the 353/355-keV transitions in DB2 and the 461-keV transition in DB1 confirms the placement of DB5 to be above DB1 and DB2. The lack of a 708-keV linking transition to Band 1 and the 827-keV transition in Band 1 in Fig. 4(b) suggests that the bandhead of DB5 does not feed into the  $22^+$  state in DB1. The nonobservation of states above the 798-keV transition in Band 2 also suggests that DB5 does not feed into the higher lying states in Band 2.

### 7. DB3 and DB4

Figure 4(c) shows a spectrum resulting from a double gate on the 169- and 267-keV transitions in DB3. The 153- and 755-keV transitions are not present in the spectrum, suggesting that they belong to a parallel cascade. Figure 4(c) also shows that low-lying members of Band 2 (552, 539, and 680 keV) are visible in the spectrum, as is the 802-keV transition, which has been assigned to link the two bands. The spectrum in Fig. 4(d) is an expanded view of the spectrum in Fig. 4(c) and shows the weak transitions assigned to DB4. This dipole band is tentatively established to feed into DB3; however, no linking

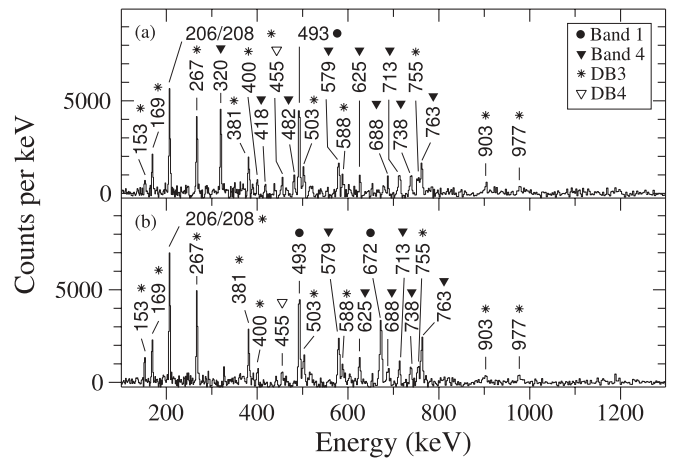


FIG. 3. Background-subtracted double-gated coincidence spectra of  $^{144}\text{Dy}$  recorded with the JURIGAM array. Only the most prominent  $\gamma$  rays are indicated. Spectrum (a) corresponds to a double gate on the 672- and 859-keV transitions and (b) corresponds to a double gate on the 751- and 427-keV transitions.

transitions were established in this work. The  $M1$  character assigned to the intense low-energy transitions in DB3 is taken from the DCO ratios in Ref. [12]. In contrast, the DCO ratios measured in this work for these  $M1$  transitions give an average value of 0.88(2), which implies a high degree of quadrupole mixing. This may be associated with the competing rotational mechanisms responsible for the states observed in the band (see Sec. IV A7). The discrepancy between the DCO results from this work and that in Ref. [12], however, is not fully understood.

### B. $^{144}\text{Dy}$ lifetime investigation

In this work, lifetime measurements were made from the analysis of RDDS data, using recoil gating with the Köln differential plunger [18]. For each of the eight target-to-degrader distances, data were sorted into asymmetric matrices comprising spectra from JURIGAM Ring 2 versus Ring 3 at backward angles of  $134^\circ$  and  $108^\circ$ , respectively. Gates were set across both components of the photopeaks feeding the transition of interest in Ring 3 and the Ring 2 spectra were projected for lifetime analysis. The spectra obtained for six of the eight distances for two of the transitions measured in Band 1 are shown in Figs. 5 and 6, with the fully Doppler shifted and degraded peaks marked for comparison.

Figure 5 shows the recoil-gated coincidence spectra obtained from a summation of gates on the 665-, 725-, and 761-keV transitions in Band 1. Both the 610- and 649-keV fully-shifted and degraded  $\gamma$  rays, required to extract the lifetime of the  $8^+$  state in Band 1, can be seen at six of the eight target-to-degrader distances. The 772-keV  $\gamma$  ray is also coincident with a 610-keV contaminant transition in  $^{143}\text{Tb}$  [30], which was also highly populated in this experiment, and for this reason it was not included in the gate summation.

Figure 6 shows the recoil-gated coincidence spectra produced from a summation of gates on the 610-, 665-, 725-, and 772-keV transitions, for the lifetime analysis of the  $6^+$  state

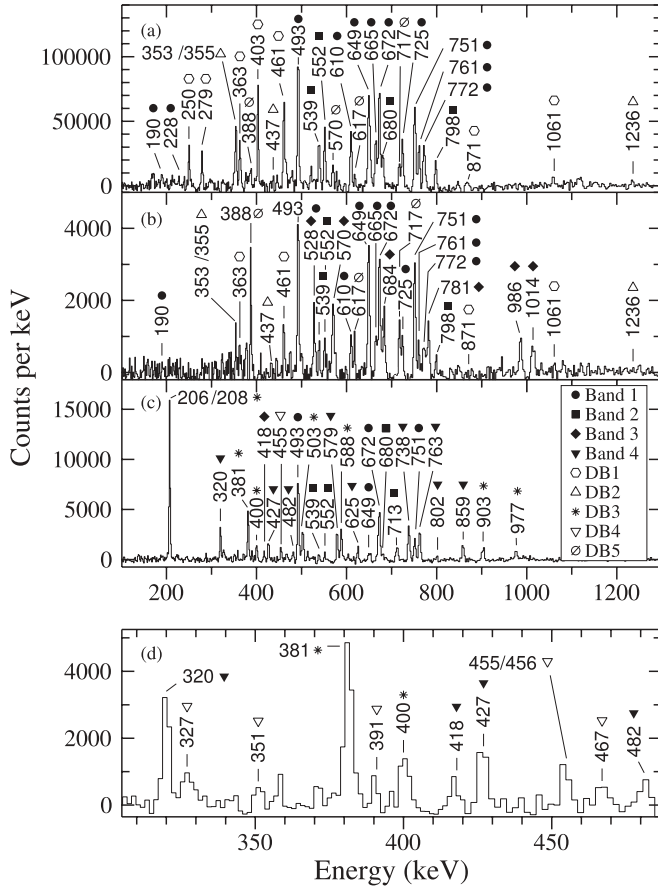


FIG. 4. Background-subtracted coincidence spectra of  $^{144}\text{Dy}$  recorded with the JUROGAM array. Only the most prominent  $\gamma$  rays are indicated. Spectrum (a) shows a single gate on the 422-keV transition in DB1 and spectrum (b) shows a double gate on the 506- and 570-keV transitions in DB5. Spectra (c) and (d) show a double gate on the 169- and 267-keV transitions in DB3, where (d) shows an expanded view of the spectrum for clarity.

in Band 1. Again, the 761-keV transition was not included in the gate owing to its coincidence with a 752-keV contaminant  $\gamma$  ray in  $^{142}\text{Gd}$  [4]. The spectra clearly show the fully Doppler shifted and degraded components of the 751- and 761-keV transitions. Although the intensity of the 761-keV  $\gamma$  ray is

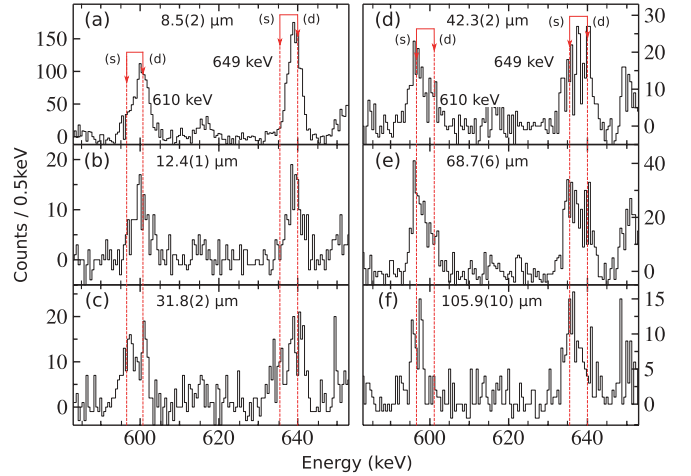


FIG. 5. (Color online) Sample recoil-gated  $\gamma$ - $\gamma$  coincidence spectra for six target-to-degrader distances obtained from a summation of gates on the 665-, 725-, and 761-keV transitions in Band 1. The splitting of the 610- and 649-keV peaks into their fully shifted (s) and degraded (d) components in the JUROGAM detectors at a backward angle of  $134^\circ$  are indicated. No Doppler correction has been applied to the spectra.

not directly required for the analysis of the lifetime of the  $6^+$  state, the overlap of its fully Doppler shifted component with the degraded component of the 751-keV transition required that it was measured. Similar spectra were produced for the analysis of the  $10^+$  and  $12^+$  levels in Band 1 and the  $10^+$  level in Band 2. These were achieved by sums of gates on the 725- and 761-keV transitions, the 761- and 772-keV transitions, and the 680- and 798-keV transitions, respectively. Table II shows the normalized intensities of the fully-shifted photopeaks at each target-to-degrader distance for each transition measured. The decay curves for the fully Doppler shifted components of each of the five levels measured, along with their calculated lifetimes, are shown in Figs. 7 and 8, for Bands 1 and 2, respectively. The lifetime values measured in this work are discussed in Sec. IV B.

It was possible to observe data for many other transitions given in Table I; however, the target-to-degrader distances used in the experiment were not optimal for determining the lifetimes of these states. For example, it is seen that the

TABLE II. Normalized fully shifted intensities of the observed  $\gamma$  rays in Bands 1 and 2. Values are quoted as percentages of the full photopeak intensity across both fully Doppler shifted and degraded components.

Distance ( $\mu\text{m}$ )	Normalized fully shifted intensities $A_s$ (%)				
	$6^+$ (751 keV)	$8^+$ (649 keV)	$10^+$ (610 keV)	$12^+$ (665 keV)	$10^+$ (552 keV)
6.4(1)	0(1)	0(2)	3.3(32)	18(4)	0(3)
8.5(2)	0(1)	0(1)	3.3(13)	18(3)	0(1)
12.4(1)	0(7)	0(11)	9.3(71)	29(7)	0(7)
22.9(2)	0.3(23)	5.8(39)	27(8)	36(8)	0(7)
31.8(2)	14(4)	38(5)	46(5)	67(8)	0(12)
42.3(2)	26(3)	42(5)	58(7)	100(18)	20(4)
68.7(6)	38(3)	55(5)	76(8)	100(14)	20(4)
105.9(10)	43(6)	71(11)	100(21)	100(11)	22(7)

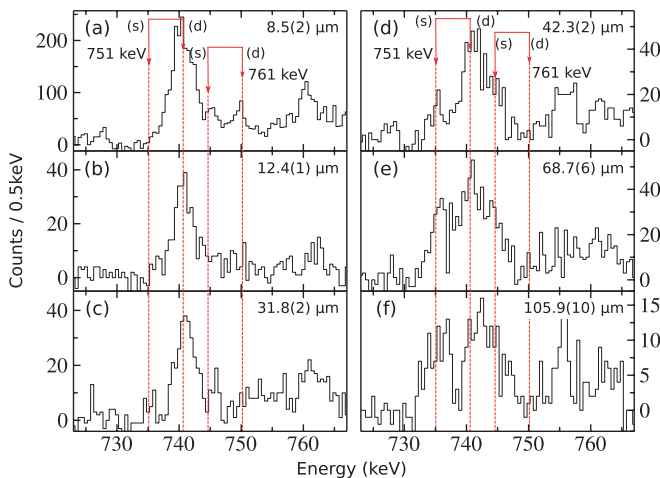


FIG. 6. (Color online) Sample recoil-gated  $\gamma$ - $\gamma$  coincidence spectra for six target-to-degrader distances obtained from a summation of gates on the 610-, 665-, 725-, and 772-keV transitions in Band 1. The fully shifted (s) and degraded (d) components of the 751- and 761-keV photopeaks in the JUROGAM detectors at a backward angle of  $134^\circ$  are highlighted. No Doppler correction has been applied to the spectra.

320-keV  $\gamma$  ray in Band 4 and the 528-keV  $\gamma$  ray in Band 2 do not show a fully Doppler shifted component, even at the maximum distance of  $100 \mu\text{m}$ . In this instance it is impossible to determine an exact lifetime for a nuclear state. However, if it is observed that the level of interest does not have any

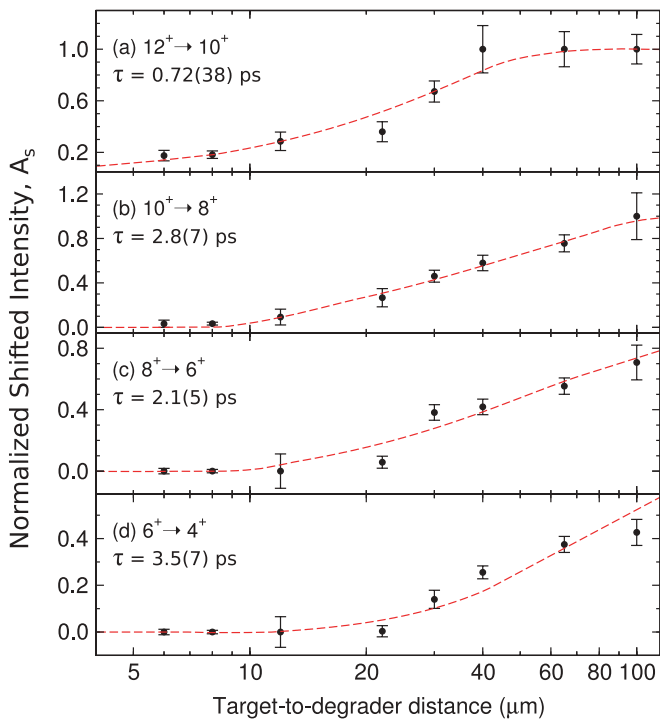


FIG. 7. (Color online) Decay curves and lifetimes for the four low-lying transitions of Band 1. Shown are the decay curves for (a) the 665-keV transition, (b) the 610-keV transition, (c) the 649-keV transition, and (d) the 751-keV transition. The dotted lines are drawn to guide the eye.

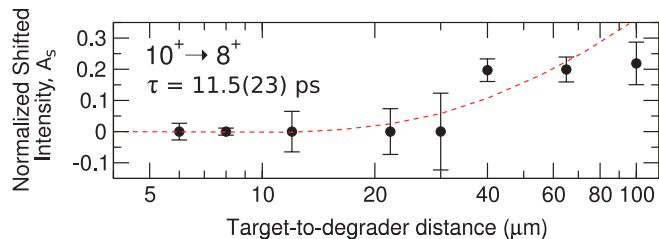


FIG. 8. (Color online) Decay curve and lifetime for 552-keV transition depopulating the  $10^+$  state in Band 2. The dotted line is drawn to guide the eye.

long-lived feeding components, it is possible to set a lower limit from this analysis, in this instance  $\sim 10$  ps. An upper limit may also be deduced based upon the geometry of the detector array and the speed with which the recoils leave the focus of the JUROGAM detector array upon entering RITU, by assuming that the full intensity of the decay is measured at the target position. The maximum distance that a recoil can move before leaving the focus of the JUROGAM array is  $\sim 15$  cm. Therefore, if the recoils enter RITU with a velocity  $v/c = 0.032(2)$ , only excited states with lifetimes less than  $\sim 16$  ns will have the full intensity of their decay detected in the rings at backward angles. The 528-keV  $\gamma$  ray depopulating the excited  $10^+$  state in Band 2 was observed to satisfy these criteria, and, consequently, limits were set on its lifetime. This has allowed a comparison to be made with the lifetimes of the analogous levels observed in the lower mass even-even isotones (see Sec. IV B).

It was also possible to observe high-lying rotational transitions in the fully Doppler shifted component at the smallest distances measured ( $6.4 \rightarrow 12.4 \mu\text{m}$ ). These states, such as those from which the 1061-, 871-, 437-, and 1236-keV  $\gamma$  rays depopulate in DB1 and DB2, have lifetimes too small to be measured with the RDDS technique with the distances employed in this experiment. However, an upper limit on the lifetimes can be set at  $\sim 1$  ps, if only the fully Doppler shifted peak is present at  $12.4 \mu\text{m}$ , and it is seen that there are no long-lived states feeding the level of interest.

#### IV. DISCUSSION

The light-mass rare-earth nuclei around  $^{144}\text{Dy}$  lie in a transitional region where the nuclear shape has been observed to undergo many changes [29]. Above the  $N = 82$  shell closure, nuclei are known to exhibit significant deformation as they evolve away from sphericity. This deformation results from the strongly downward sloping  $h_{11/2}$  proton intruder orbitals, which favor prolate deformations. However, below  $N = 82$ , the  $h_{11/2}$  neutron intruder orbitals, which favor an oblate deformation, start to compete with these prolate  $h_{11/2}$  proton orbitals. This competition can result in the population of triaxially deformed nuclear shapes [31]. It has also been well documented that the  $N = 82$  isotones in this region are influenced by the presence of the  $Z = 64$  subshell closure [32], which would favor a less-deformed nuclear shape. However, for the extremely neutron deficient nuclei well below the  $N = 82$  shell closure, strong mid-shell proton deformations

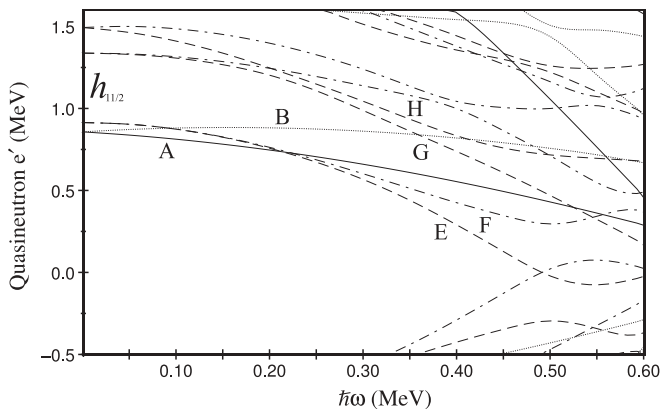


FIG. 9. Quasineutron Routhians as a function of rotational frequency in  $^{144}\text{Dy}$ , calculated with deformation parameters  $\beta_2 = 0.20$ ,  $\beta_4 = 0.04$ , and  $\gamma = -25^\circ$ . The following convention is used for the levels: solid line:  $(\pi, \alpha) = (+, +\frac{1}{2})$ , dotted line:  $(\pi, \alpha) = (+, -\frac{1}{2})$ , dashed-dotted line:  $(\pi, \alpha) = (-, +\frac{1}{2})$ , and dashed line:  $(\pi, \alpha) = (-, -\frac{1}{2})$ .

persist, leading to a variety of different phenomena. The even-even isotone  $^{142}\text{Gd}$ , which lies in this region, appears to reflect much of the structural behavior observed in  $^{144}\text{Dy}$  and has been rigorously studied over the past 15 years [2–8].

Recent calculations by Möller and Bengtsson [1] have predicted that the  $^{144}\text{Dy}$  ground-state deformation contains a large degree of triaxiality, with deformation parameters ( $\beta_2 = 0.20$ ,  $\beta_4 = 0.04$ ,  $\gamma = -25^\circ$ ). Woods-Saxon cranked shell model (CSM) calculations have been performed using these parameters to help assign configurations to the experimental behavior of the bands observed in  $^{144}\text{Dy}$ . Figures 9 and 10 show the theoretical quasiparticle Routhians for neutrons and protons, respectively. The Routhians are described by their quantum numbers parity ( $\pi$ ) and signature ( $\alpha$ ). The standard convention for labeling levels has been used: The negative-parity states E and F correspond to  $(\pi, \alpha) = (-, -\frac{1}{2})_1$

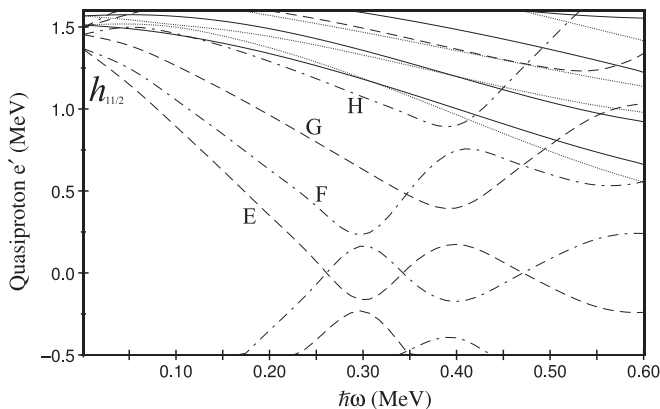


FIG. 10. Quasiproton Routhians as a function of rotational frequency in  $^{144}\text{Dy}$ , calculated with deformation parameters  $\beta_2 = 0.20$ ,  $\beta_4 = 0.04$ , and  $\gamma = -25^\circ$ . The following convention is used for the levels: solid line:  $(\pi, \alpha) = (+, +\frac{1}{2})$ , dotted line:  $(\pi, \alpha) = (+, -\frac{1}{2})$ , dashed-dotted line:  $(\pi, \alpha) = (-, +\frac{1}{2})$ , and dashed line:  $(\pi, \alpha) = (-, -\frac{1}{2})$ .

TABLE III. Signature ( $\alpha$ ) and parity ( $\pi$ ) assignments for lowest lying Nilsson proton and neutron orbitals around the Fermi surface in  $^{144}\text{Dy}$ . The signature and parity are defined by  $(\alpha, \pi)_n$ , where  $n$  describes the number of times a specific  $(\alpha, \pi)$  configuration has occurred.

Label	$(\alpha, \pi)_n$	$nl_j^\pi$ shell	Nilsson orbital
Protons $\pi$			
E	$(-, -\frac{1}{2})_1$	$1h_{11/2}^-$	[532]5/2 <sup>-</sup>
F	$(-, +\frac{1}{2})_1$	$1h_{11/2}^-$	[532]5/2 <sup>-</sup>
G	$(-, -\frac{1}{2})_2$	$1h_{11/2}^-$	[523]7/2 <sup>-</sup>
H	$(-, +\frac{1}{2})_2$	$1h_{11/2}^-$	[523]7/2 <sup>-</sup>
A	$(+, +\frac{1}{2})_1$	$(2d_{3/2}^+)$	[(411)1/2 <sup>+</sup> ]
B	$(+, -\frac{1}{2})_1$	$(2d_{3/2}^+)$	[(411)1/2 <sup>+</sup> ]
Neutrons $\nu$			
E	$(-, -\frac{1}{2})_1$	$1h_{11/2}^-$	[514]9/2 <sup>-</sup>
F	$(-, +\frac{1}{2})_1$	$1h_{11/2}^-$	[514]9/2 <sup>-</sup>
G	$(-, -\frac{1}{2})_2$	$1h_{11/2}^-$	[505]11/2 <sup>-</sup>
H	$(-, +\frac{1}{2})_2$	$1h_{11/2}^-$	[505]11/2 <sup>-</sup>
A	$(+, +\frac{1}{2})_1$	$2d_{3/2}^+$	[400]1/2 <sup>+</sup>
B	$(+, -\frac{1}{2})_1$	$2d_{3/2}^+$	[400]1/2 <sup>+</sup>

and  $(-, +\frac{1}{2})_1$ , and the states G and H refer to  $(\pi, \alpha) = (-, -\frac{1}{2})_2$  and  $(-, +\frac{1}{2})_2$ , respectively. The positive-parity states A and B are denoted by  $(\pi, \alpha) = (+, +\frac{1}{2})_1$  and  $(+, -\frac{1}{2})_1$ , respectively. The Nilsson model predicts the negative-parity states to arise mostly from the  $h_{11/2}$  intruder orbitals, at low rotational frequencies, with a small contribution from the  $f_{7/2}$  orbital at higher frequencies. The positive-parity states are predicted to contain contributions from the  $d_{3/2}$ ,  $s_{1/2}$ ,  $g_{7/2}$ , and  $d_{5/2}$  subshells. Table III summarizes the lowest energy neutron and proton states and the Nilsson orbitals around the Fermi surface that they have been assigned in the current work. These assignments have been made from comparisons with excited states in the neighboring nuclei.

### A. Configuration of bands

Figure 11 shows the experimental aligned angular momentum (alignment),  $i_x$  [33], as a function of rotational frequency for Bands 1–4 in  $^{144}\text{Dy}$  and  $^{142}\text{Gd}$  [4]. A reference band with Harris parameters  $\mathfrak{S}_0 = 6.0\hbar^2/\text{MeV}$  and  $\mathfrak{S}_1 = 26.0\hbar^4/\text{MeV}^3$  has been subtracted from each band [34]. These Harris parameters result in zero alignment at low spin for the ground-state band in  $^{144}\text{Dy}$ . Figure 12(a) shows the excitation energies of the states as a function of spin, with a collective rigid-rotor reference of  $0.01I(I+1)$  subtracted to account for the core rotation of the nucleus. This plot shows which excited levels are yrast for a given spin. The experimental Routhian plot, Fig. 12(b), shows the energy of the states in the rotating frame,  $e'$ , as a function of nuclear rotation, emphasizing the rotational frequency at which the bands are observed to align or undergo a band crossing. These plots have been used in conjunction with the CSM calculations to assign configurations to the new bands presented in this work.

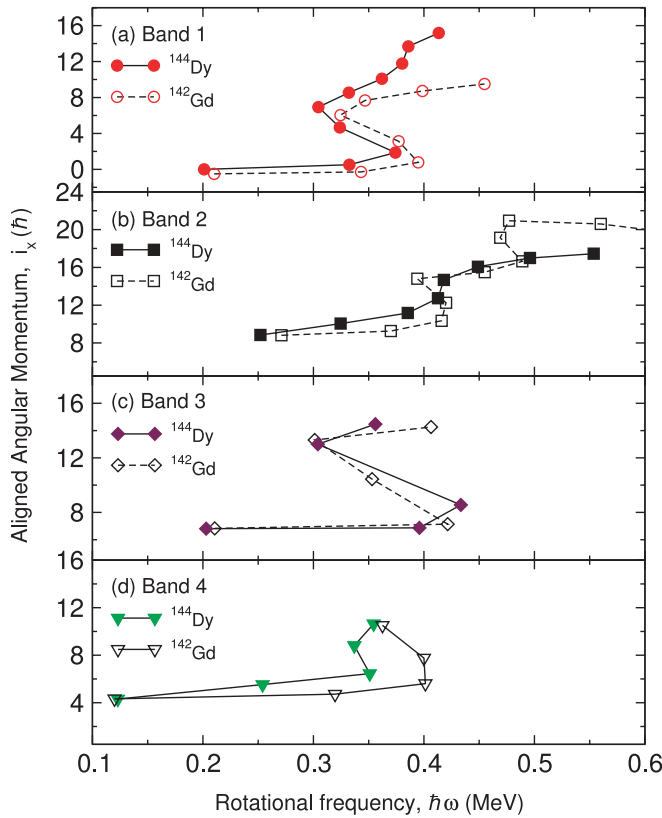


FIG. 11. (Color online) Experimental alignments for (a) Band 1, (b) Band 2, (c) Band 3, and (d) Band 4 in  $^{144}\text{Dy}$  (closed symbols) and  $^{142}\text{Gd}$  (open symbols) from Ref [4].

### 1. Band 1

In the work performed here we have assigned Band 1 to what was previously described as an “antimagnetic rotational” band built upon a neutron quasiparticle alignment [12]. The assignment made in this work is based mainly upon comparisons with the alignment gains observed in the neighboring nucleus  $^{142}\text{Gd}$ . Band 1 in  $^{144}\text{Dy}$  shows a gain in alignment of  $\Delta i_x \approx 7.5\hbar$  at  $\hbar\omega \approx 0.34$  MeV [see Fig. 11(a)]. The yrast band in  $^{142}\text{Gd}$  shows a similar alignment gain of  $\Delta i_x \approx 7.0\hbar$  at a rotational frequency of  $\approx 0.36$  MeV, which was assigned to a proton- $h_{11/2}$  crossing [4]. The quasiproton CSM calculations shown in Fig. 10 suggest that this might result from the first observed  $\pi(\text{EF})$  proton crossing at  $\hbar\omega \approx 0.31$  MeV. However, the theoretical CSM alignment of  $\sim 9.3\hbar$  for these orbitals is larger than the experimental value calculated from Fig. 12(b). In addition, the excitation energy minus rigid-rotor plots in Fig. 12(a) show that the configuration of Band 1 above the alignment is no longer yrast, being crossed by Band 2 (see later). The alignment observed in Band 1 in this work has therefore been attributed to the unfavored proton configuration,  $\pi(\text{FG})$ , and not  $\pi(\text{EF})$ . The  $\pi(\text{FG})$  configuration lies higher in energy than the first observed crossing,  $\pi(\text{EF})$ . This would account for the reduced intensity feeding the  $8^+$  level in Band 1 from states above this first alignment, relative to Band 2. The experimental alignment gain for Band 1 can be understood by assuming two paired protons are broken by rotation and excited into the  $\alpha = +1/2$  and  $\alpha = -1/2$  signatures of the

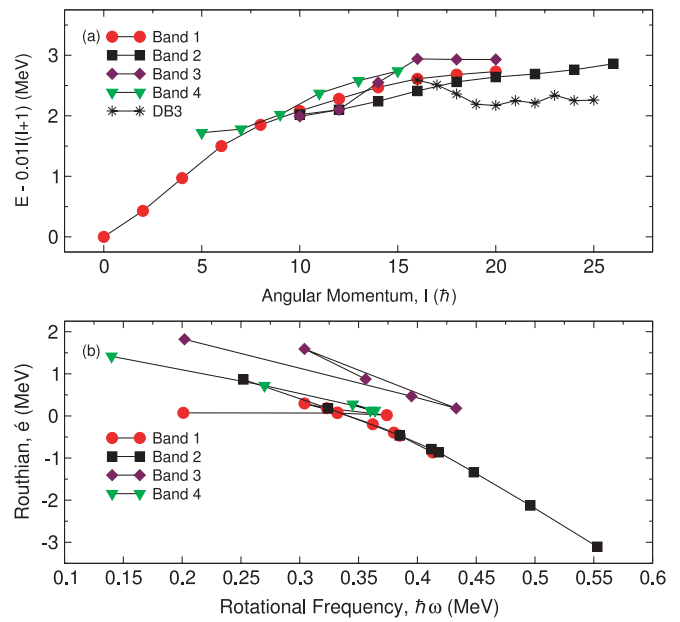


FIG. 12. (Color online) Experimental excitation energy minus a rigid-rotor reference (a) and Routhian (b) plots for  $^{144}\text{Dy}$ . A rigid-rotor reference of  $0.01I(I+1)$  has been subtracted from the observed energies in (a) to emphasize the band crossings.

[532]5/2<sup>-</sup> and [523]7/2<sup>-</sup> Nilsson orbitals, respectively. These states are among the lowest energy Nilsson orbitals above the Fermi surface. A second alignment is observed at higher frequencies in Band 1 of  $^{144}\text{Dy}$ , but not in  $^{142}\text{Gd}$ , which, instead, is seen to take on the properties of a more perfect rotor, where the difference in energy of the excited states remains constant as a function of increasing spin [5]. However, as the previous work on  $^{142}\text{Gd}$  [4] was only able to establish four levels above the  $10^+$  state in Band 1, it was not possible to determine whether any crossings occurred at higher rotational frequencies. The second alignment gain in Band 1 in  $^{144}\text{Dy}$  of  $\Delta i_x \approx 5\hbar$  occurs at a rotational frequency of  $\hbar\omega \approx 0.38$  MeV. This crossing is likely to be the second allowed unfavored proton crossing,  $\pi(\text{EH})$  (see Fig. 10), and not the first allowed favored neutron crossing  $\nu(\text{EH})$ , which is expected to occur at a much larger frequency as shown in Fig. 9. The  $\pi(\text{EH})$  alignment in Band 1 is assigned to the  $\alpha = -1/2$  and  $\alpha = +1/2$  signatures of the [532]5/2<sup>-</sup> and [523]7/2<sup>-</sup> Nilsson orbitals, respectively. Table IV summarizes the underlying configurations and crossings at various frequencies assigned to Band 1 as well as Bands 2, 3, DB1, and DB2, as will be discussed later.

### 2. $I^\pi = 10^+$ configurations

Previous experimental work has been performed to obtain  $g$  factors for the two rotational bands based on  $I^\pi = 10^+$  configurations in both  $^{140}\text{Sm}$  [6] and  $^{142}\text{Gd}$  [8]. In the analysis of these experiments in Ref. [6], combined with comparisons of the band structures with those of the neighboring nuclei [5], the  $10^+$  bandhead states were assigned  $\pi(h_{11/2})^2$  and  $\nu(h_{11/2})^{-2}$  configurations. A similar comparison has been

TABLE IV. Configurations assigned to the bands in  $^{144}\text{Dy}$  in this work.  $\hbar\omega_c$  corresponds to the frequency of the observed quasiparticle crossing,  $\Delta i_x$  is the gain in aligned angular momentum at the given crossing frequency.

Band	$\hbar\omega_c$ (MeV)	Low-frequency $i_x$ ( $\hbar$ )	$\Delta i_x$ ( $\hbar$ )	Configuration	Crossing
1	0.34	–	$\approx 7.5$	–	$\pi(\text{FG})$
	0.38	–	$\approx 5.0$	$\pi(\text{FG})$	$\pi(\text{EH})$
2	0.34	–	$\approx 9.0$	–	$\pi(\text{EF})$
	0.42	–	$\approx 5.0$	$\pi(\text{EF})$	$\pi(\text{GH})$
3	–	$\approx 6.2$	–	–	$\nu(\text{EH})$
	0.34	–	$\approx 8.0$	$\nu(\text{EH})$	$\pi(\text{EF})$
4	–	$\approx 3.5$	–	–	$\pi(\text{EA})$
	0.35	–	$\approx 6.0$	$\pi(\text{EA})$	–
DB1	–	–	–	$\pi(\text{EF})$	$\nu(\text{EF})$
DB2	–	–	–	$\pi(\text{FG})$	$\nu(\text{EF})$

made in this work for  $^{144}\text{Dy}$ , between the excited states above the two  $10^+$  levels in Bands 2 and 3 and the ground-state sequences observed in the core nuclei  $^{142}\text{Gd}$  [4] with  $Z - 2$ ,  $N = 78$ ,  $^{143}\text{Tb}$  [30] with  $Z - 1$ ,  $N = 78$ ,  $^{145}\text{Dy}$  [35] with  $Z = 66$ ,  $N + 1$ , and  $^{146}\text{Dy}$  [36] with  $Z = 66$ ,  $N + 2$ . These two  $10^+$  bands in  $^{144}\text{Dy}$  are thought to be analogous to those observed in  $^{140}\text{Sm}$  and  $^{142}\text{Gd}$ . Figure 13 shows the relevant parts of the level schemes for  $^{144}\text{Dy}$ ,  $^{142}\text{Gd}$ ,  $^{143}\text{Tb}$ ,  $^{145}\text{Dy}$ , and  $^{146}\text{Dy}$ .

In  $^{144}\text{Dy}$ , the most energetically favorable method of forming two additional units of angular momentum above a  $\pi(h_{11/2})^2$  state would arise from the rotational excitation of the  $N = 78$  four-neutron-hole core. This is analogous to the method by which low-lying excited states are generated in the ( $Z - 2$ ,  $N = 78$ ) neighboring isotone  $^{142}\text{Gd}$ . The similarity in the energy level spacings up to the  $16^+$  state in the

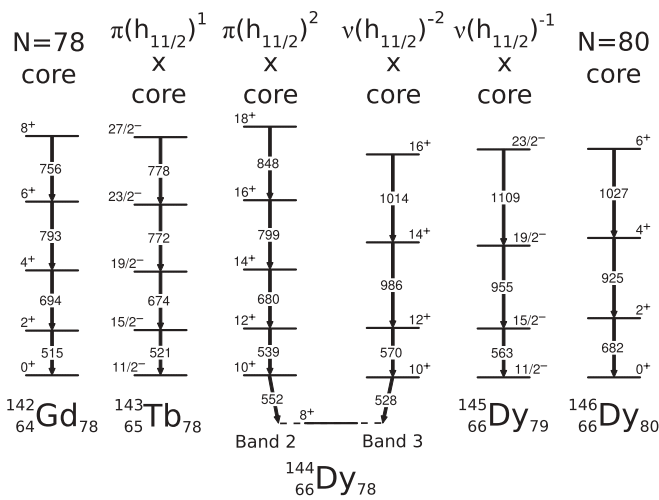


FIG. 13. Comparisons between bands built upon the  $10^+$  states in  $^{144}\text{Dy}$  and the ground-state configurations in  $^{142}\text{Gd}$  [4],  $^{143}\text{Tb}$  [30],  $^{145}\text{Dy}$  [35], and  $^{146}\text{Dy}$  [36]. The excitation energies of the  $0^+$  ground states in  $^{146}\text{Dy}$  and  $^{142}\text{Gd}$  and the excited  $11/2^-$  states in  $^{143}\text{Tb}$  and  $^{145}\text{Dy}$  have all been normalized to the excitation energy of the respective  $10^+$  states in  $^{144}\text{Dy}$ .

two-quasiparticle Band 2 in  $^{144}\text{Dy}$  in Fig. 13 and those of the  $0^+$  band in  $^{142}\text{Gd}$  and  $11/2^-$  band in  $^{143}\text{Tb}$  suggest that the  $I^\pi = 10^+$  state in Band 2 arises from the  $\pi(h_{11/2})^2$  configuration coupled to the  $N = 78$  core. Deviations in this comparison, which become more apparent as the nuclear spin increases, are assumed to be the result of the changing deformation of the nucleus in each instance. These changes are driven by the polarizing effects of the different numbers of excited quasiprotons in each isotone.

Excited states above a two-quasineutron  $\nu(h_{11/2})^{-2}$  excitation are expected to result from the contribution of the two remaining neutron holes below the  $N = 82$  shell closure. This scenario may be expected to result in larger energy spacings above the  $I^\pi = 10^+$  state, similar to those in the ground-state band of the ( $Z = 66$ ,  $N - 2$ ) isotope  $^{146}\text{Dy}$ . These irregularly large energy spacings are indeed observed in the band to the right in Fig. 13. The similarity of Band 3 in  $^{144}\text{Dy}$  to the higher mass Dy isotopes suggests that this  $I^\pi = 10^+$  state arises from the excited  $\nu(h_{11/2})^{-2}$  configuration coupled to the  $N = 80$  core. Again, differences in the observed level schemes are assumed to arise from core polarization effects, resulting in changes in the nuclear shape.

Similar comparisons were attempted in Ref. [12]; however, that resulted in the now assigned Band 1 being attributed to the  $\nu(h_{11/2})^{-2}$  configuration (right-hand side of Fig. 13). In addition, Band a in Ref. [12] (Band 3 in this work) was previously not compared as a result of a different ordering of transitions. The new order of transitions established in this work reveal a remarkable correspondence to that of the two core nuclei  $^{145}\text{Dy}$  and  $^{146}\text{Dy}$ .

### 3. Band 2

Comparisons of the states in Band 2, built on the  $10^+$  level in  $^{144}\text{Dy}$ , with the ground-state sequences in the adjacent  $N = 78$  isotones confirm the two-quasiproton  $\pi(h_{11/2})^2$  nature of the bandhead state. With an initial alignment of  $i_x \approx 9\hbar$ , Band 2 has been assigned to be based upon the two-quasiproton configuration,  $\pi(\text{EF})$ , corresponding to protons in both signatures of the  $[532]5/2^-$  Nilsson orbital. The theoretical CSM alignment for this configuration is  $\sim 9.3\hbar$  (see Fig. 10). Figure 12(a) shows that Band 2 is yrast above the first alignment, which would be expected for a band based on the first favored crossing shown in the CSM (Fig. 10). Band 2 is observed to undergo an alignment gain  $\Delta i_x \approx 5\hbar$  at  $\hbar\omega \approx 0.42$  MeV. Figure 11(b) shows that the equivalent band in  $^{142}\text{Gd}$  is subject to the same alignment gain at  $\hbar\omega \approx 0.41$  MeV.

The theoretical CSM calculations in Figs. 9 and 10 show that the neutron  $\nu(\text{EF})$  crossing is expected at  $\hbar\omega \approx 0.52$  MeV, and the two proton crossings,  $\pi(\text{EH})$  and  $\pi(\text{FG})$  at  $\hbar\omega \approx 0.4$  MeV. As the initial configuration of Band 2 involves the favored  $\pi(\text{EF})$  crossing, the second proton crossings are both expected to be blocked. This may suggest that the second alignment most likely arises from the first observed favored neutron crossing, for which the CSM calculations give a theoretical alignment of  $\sim 5.3\hbar$ . Although this appears to occur at a much larger rotational frequency, it is possible that changes

in the nuclear shape and  $\gamma$  softness, as a result of the first proton crossing, may lower the rotational frequency at which this crossing is seen to occur. A recent study on the triaxial rotation in  $^{142}\text{Gd}$  [7] has examined the maximum spin values that can be generated from all the possible low-energy configurations of neutrons and protons for the positive-parity band, analogous to Band 2 in  $^{144}\text{Dy}$ . In that study, the only configuration that could result in the large values of spin observed in Band 2 in  $^{142}\text{Gd}$ , up to  $I = 34^+$ , is that of a four-quasiproton excitation. In this instance, the only available quasiproton configuration involves the  $\pi(\text{GH})$  states, which are substantially lowered in energy at  $\hbar\omega \approx 0.41$  MeV. This work tentatively assigns the alignment in Band 2 to the  $\pi(\text{GH})$  crossing based upon the calculations in Ref. [7]. This alignment results from the excitation of a pair of protons into the  $\alpha = +1/2$  and  $\alpha = -1/2$  signatures of the  $[523]7/2^-$  Nilsson orbitals, respectively. It is understood, however, that further study with higher statistics is required to determine whether Band 2 in  $^{144}\text{Dy}$  continues to higher spin, as seen in  $^{142}\text{Gd}$ . In this case, further theoretical calculations are required with the inclusion of triaxiality to determine whether the configuration tentatively assigned here is correct.

#### 4. Band 3

The comparison of excited states above the  $10^+$  level in Band 3 of  $^{144}\text{Dy}$  with the ground-state sequences in the adjacent  $Z = 66$  isotopes revealed a two-quasineutron  $\nu(h_{11/2})^{-2}$  configuration for the bandhead state. With an initial alignment of  $i_x \approx 6.2\hbar$  in Band 3 [see Fig. 11(c)], the bandhead state is assigned to be based upon the unfavored two-quasineutron configuration,  $\nu(\text{EH})$ , corresponding to neutrons in the  $\alpha = -1/2$  and  $\alpha = +1/2$  signatures of the  $[514]9/2^-$  and  $[505]11/2^-$  Nilsson orbitals, respectively. These Nilsson states are among the lowest in energy above the neutron Fermi surface. Figure 12(a) shows that Band 3 is largely nonyrast at high frequency, and the RDDS data (see Sec. IV B) reveal a relatively large value for the lifetime of this  $10^+$  state. Figure 11(c) shows Band 3 starts to undergo a crossing with  $\Delta i_x \approx 8.0\hbar$  at  $\hbar\omega \approx 0.34$  MeV.  $^{142}\text{Gd}$  shows a similar alignment at the same rotational frequency, but previous work did not assign this crossing to a specific configuration. The alignment gain in  $^{144}\text{Dy}$  is tentatively assigned to the favored proton crossing,  $\pi(\text{EF})$ . The reason for this assignment is because Band 3 is fed from higher energies by dipole bands assumed to be based upon four quasiproton excitations. The theoretical CSM alignment gain for this crossing is larger than that measured experimentally from Fig. 12. However, the full backbend is not observed in the present work and it may be that higher spin states continue to align at larger rotational frequencies. More data at higher rotational frequencies are needed to fully confirm this prediction.

#### 5. Band 4

Low-lying bands, built upon  $5^-$  and  $7^-$  states, have been found to occur systematically in nuclei in this region. For example, these  $5^-$  and  $7^-$  states are assigned  $\nu(h_{11/2}^{-1}s_{1/2}^{-1})$  and  $\nu(h_{11/2}^{-1}d_{3/2}^{-1})$  configurations, respectively, in  $^{146}\text{Dy}$  [36].

The alignment plot for Band 4 in  $^{144}\text{Dy}$  and the equivalent band in  $^{142}\text{Gd}$  [see Fig. 11(d)] shows an initial alignment of  $\approx 3\hbar-4\hbar$  at low rotational frequencies,  $\hbar\omega \approx 0.12$  MeV. The similarity in the low-spin alignment observed in this work and the alignment of the analogous band in  $^{142}\text{Gd}$  [4] gives further evidence for the rearrangement of the 579- and 763-keV transitions in Band 4 in the present work, over that in Ref. [12]. In this work the  $7^-$  configuration in  $^{144}\text{Dy}$  has been assigned to the excited two-quasineutron configuration based upon a  $\nu(\text{EA})$  occupancy, comprising the  $[514]9/2^-$  and  $[400]1/2^+$  Nilsson orbitals. Both bands in  $^{144}\text{Dy}$  and  $^{142}\text{Gd}$  appear to undergo similar alignment gains of  $\Delta i_x \approx 6\hbar$ , but at different frequencies. In each instance, both bands are fed directly by a dipole band assumed to have a configuration comprising excited proton and neutrons in  $h_{11/2}$  orbitals. In this work, therefore, it is assumed that the observed alignments result from excitations of nucleons in  $h_{11/2}$  orbitals, although specific configurations have not been assigned as more statistics are required to establish all of the higher lying excited states.

#### 6. Dipole bands: DB1 and DB2

The dipole bands DB1 and DB2 have no directly equivalent bands in  $^{142}\text{Gd}$ . However, there is a dipole band in  $^{142}\text{Gd}$ , which occurs at a similar excitation energy [4]. This single dipole band in  $^{142}\text{Gd}$  was assigned a  $\nu(h_{11/2})^{-2}\pi(h_{11/2})^2$  configuration [2], which is consistent with the fact that the bandhead was observed at an excitation energy of  $\sim 6$  MeV, approximately twice that of the  $\nu(h_{11/2})^{-2}$  and  $\pi(h_{11/2})^2$   $10^+$  two-quasiparticle excitations. The same addition of two-quasiparticle excitation energies is true for DB1 and DB2 observed in  $^{144}\text{Dy}$  in this work (see Fig. 1), and it is tentatively assumed that both these bands arise from  $\nu(h_{11/2})^{-2}\pi(h_{11/2})^2$  configurations, with different underlying Nilsson orbitals contributing in each instance. DB2 is seen to feed predominantly into Band 2, and it may therefore have a  $\pi(\text{EF})$  component in its configuration. The aligned neutrons are assumed to arise from the  $\nu(\text{EF})$  Nilsson orbitals, which is the most energetically favored allowed configuration. DB1 feeds into Band 1 with more intensity than Band 2, and it lies higher in excitation energy than DB2. For these reasons, in this work, DB1 is tentatively assumed to be built upon the  $\pi(\text{FG})\nu(\text{EF})$  Nilsson configuration. Unfortunately, these bands were not extended high enough in rotational frequency to reveal any alignments that would aid the configuration assignments.

#### 7. Dipole band: DB3

Qualitative comparisons have recently been made to show the similarity between DB3 in  $^{144}\text{Dy}$  and the known ‘magnetic rotor’ in  $^{110}\text{Cd}$  [12]. To further assess this prediction, in the present work,  $B(M1)/B(E2)$  ratios and the ratio of the  $g$  factors to the quadrupole moment,  $|(g_k - g_r)/Q_0|$ , have been calculated for DB3. The experimental  $\Delta I = 2$  to  $\Delta I = 1$   $\gamma$ -ray intensity branching ratios allowed the calculation of the  $B(M1; I \rightarrow I - 1)/B(E2; I \rightarrow I - 2)$  values, shown in

TABLE V. Experimental  $B(M1)/B(E2)$  and  $|(g_k - g_r)/Q_0|$  values based upon a projection,  $K$  of  $16\hbar$ , with a mixing ratio of  $\delta = 0$ .

$I^\pi$	$B(M1)/B(E2) [\mu_N/(e\text{ b})]^2$	$ (g_k - g_r)/Q_0  \times 10^3 [\mu_N/(e\text{ b})]^2$
$24^-$	12.7(10)	7.9(6)
$23^-$	7.7(11)	4.4(6)
$22^-$	6.2(6)	3.1(3)
$20^-$	1.1(1)	0.40(2)

Table V, using

$$\frac{B(M1; I \rightarrow I-1)}{B(E2; I \rightarrow I-2)} = 0.697 \frac{E_\gamma^5(I \rightarrow I-2) I_\gamma(I \rightarrow I-1)}{E_\gamma^3(I \rightarrow I-1) I_\gamma(I \rightarrow I-2)}, \quad (3)$$

where  $I_\gamma$  is the relative intensity of a given transition and  $E_\gamma$  is its energy in MeV. A mixing ratio of  $\delta = 0$  was assumed in the calculations. Although the dipole transitions in DB3 appear to have a substantial amount of quadrupole admixture, variations in the value of  $\delta$  only act to reduce the magnitude of the measured  $B(M1)/B(E2)$  ratios, which further emphasize the differences seen between DB3 and that of an analogous band in  $^{142}\text{Gd}$  [2]. Figure 14 compares the  $B(M1)/B(E2)$  ratios calculated in this work for  $^{144}\text{Dy}$  with those determined for the equivalent band (denoted DB3) in  $^{142}\text{Gd}$ . The ratios determined in  $^{142}\text{Gd}$  appear to decrease with increasing spin, which is consistent with the behavior expected for a band built upon magnetic rotation [37]. The values determined in this work for  $^{144}\text{Dy}$  appear to show the opposite trend, with increasing  $B(M1)/B(E2)$  ratios with nuclear spin. A possible explanation for this difference may be a consequence of the competition between deformed nuclear rotation and magnetic dipole rotation as the mechanism through which these excited states are produced. At low spin, a larger intensity flow through the quadrupole transitions may be the result of an initial excitation driven by deformed rotation. At higher spin, an increasing contribution from magnetically driven excitations may favor a larger intensity flow through the dipole

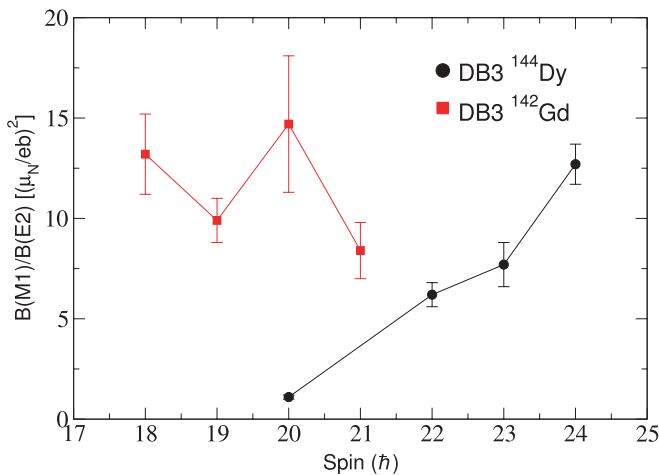


FIG. 14. (Color online) Experimental  $B(M1)/B(E2)$  ratios as a function of the nuclear spin for dipole bands DB3 in  $^{144}\text{Dy}$  and  $^{142}\text{Gd}$  from Ref. [2].

transitions. This reason for the different trends seen in  $^{144}\text{Dy}$  and  $^{142}\text{Gd}$  may be due to a larger number of valence protons in  $^{144}\text{Dy}$  driving the nucleus toward a more prolate deformation, where rotational excitations can compete with those induced by magnetic rotation. Lower spin states were observed in DB3 in  $^{142}\text{Gd}$  but not in the present work on  $^{144}\text{Dy}$ . Further experiments into whether these states are present in  $^{144}\text{Dy}$  are essential in fully understanding the extent to which each mechanism is responsible for the observed states.

The ratio of the  $g$  factors to the quadrupole moment,  $Q_0$ , in DB3 were calculated with

$$\left| \frac{(g_k - g_r)}{Q_0} \right| = \frac{5}{12K^2} \frac{B(M1) \langle IK20|I-2K \rangle^2}{B(E2) \langle IK10|I-1K \rangle^2}, \quad (4)$$

where  $K$ , the angular momentum projection onto the symmetry axis, was taken to be  $16\hbar$ .

In these calculations a value of  $Q_0 = 1.8(3) e\text{ b}$  was used based upon the lifetime measurement of the  $6^+$  state in Band 1 (see Sec. IV B). This small quadrupole moment, corresponding to a very weakly deformed structure, was reasoned to be also valid for DB3. Although it was not possible to extract quantitative lifetime measurements for DB3, it was possible to observe a long-lived “degraded component” for the 267-keV  $\gamma$  ray that feeds the  $16^-$  level, implying a small value for the quadrupole moment, similar to those measured in the ground-state band.

The equivalent dipole band observed in  $^{142}\text{Gd}$  is proposed to have the configuration  $\pi(h_{11/2})^1 \otimes \nu(g_{7/2})^{-1} \nu(h_{11/2})^{-2}$  [2]. By assuming the same configuration here for DB3, theoretical  $|(g_k - g_r)/Q_0|$  values have been calculated based upon all possible underlying Nilsson orbitals that appear around the Fermi surface (see Table VI). The theoretical results appear to overestimate the experimental  $|(g_k - g_r)/Q_0|$  values in Table V by a factor of  $\sim 10$ , with none of the configurations providing a good match. This may indicate that collective nuclear rotation is a less likely mechanism for generating the states in DB3 in  $^{144}\text{Dy}$ . However, the large dependency of these values on  $Q_0$  highlights the need for accurate lifetime measurements in this region. Similar results were achieved for the  $B(M1)/B(E2)$  measurements of DB1 and DB2, assumed to be built upon  $\pi(h_{11/2})^2 \nu(h_{11/2})^{-2}$  configurations, in  $^{142}\text{Gd}$  [2,3]. In that work, a further investigation into the lifetimes of the states in  $^{142}\text{Gd}$ , and comparison with the “shears mechanism with principal axis cranking” (SPAC) model suggested that the bands resulted from a magnetic rotation of the nucleus [3,38]. This explanation could account for why DB3 appears to be yrast in Fig. 12(a), as energy is no longer required to rotate the nucleus to large frequency; instead, a large component of the angular momentum may be generated by the closing of proton and neutron projections onto the rotation axis. Again, further experiments are required to fully assess the amount by which magnetic rotation is responsible for the observed states in DB3 in  $^{144}\text{Dy}$ .

## B. RDDS lifetimes

Lifetime measurements were made for five excited states in Bands 1 and 2 of  $^{144}\text{Dy}$ . These lifetime measurements are

TABLE VI.  $|(g_k - g_r)/Q_0|$  values for a range of Nilsson orbitals that could contribute to the configuration of DB3. A constant deformation of 1.8(3)  $e$  b has been used in each case, and only orbitals around the Fermi surface in Figs. 9 and 10 have been considered. The value for  $g_R$  in each case was taken to be  $Z/A$ .

Configuration	Nilsson orbitals	$K$	$ (g_k - g_r)/Q_0  \times 10^3$ $[\mu_N/(e \text{ b})]^2$
$\pi h_{11/2}^1 \otimes \nu g_{7/2}^{-1} \nu h_{11/2}^{-2}$	$\pi[532]5/2 \nu[404]7/2 \nu[523]7/2 \nu[514]9/2$	14	57
	$\pi[523]7/2 \nu[404]7/2 \nu[523]7/2 \nu[514]9/2$	15	42
	$\pi[514]9/2 \nu[404]7/2 \nu[523]7/2 \nu[514]9/2$	16	30
	$\pi[532]5/2 \nu[402]5/2 \nu[523]7/2 \nu[514]9/2$	13	57
	$\pi[523]7/2 \nu[402]5/2 \nu[523]7/2 \nu[514]9/2$	14	40
	$\pi[514]9/2 \nu[402]5/2 \nu[523]7/2 \nu[514]9/2$	15	28

related to the reduced transition probability of the transition using

$$\tau = \frac{8.2 \times 10^{-10}}{B(E2; I \rightarrow I-2)(1 + \alpha_{\text{tot}})E_\gamma^5}, \quad (5)$$

where  $B(E2)$  is in  $e^2 \text{ b}^2$ ,  $E_\gamma$  is in MeV and  $\tau$  is in picoseconds. The total internal conversion coefficient  $\alpha_{\text{tot}}$  for the transition was calculated using theoretical values from the BrIcc internal conversion coefficient database [39]. Transition quadrupole moments  $Q_t$  were then calculated for each of the measured levels using the relation

$$B(E2; I \rightarrow I-2) = \frac{5}{16\pi} Q_t^2 \langle IK20|I-2K \rangle^2, \quad (6)$$

with  $K = 0$ . Within the rigid-rotor rotational model framework for a triaxial nucleus, the in-band transition quadrupole moments are equal to the intrinsic quadrupole moment  $Q_0$ , which is in turn related to the deformation  $\beta_2$  via

$$Q_0 = \frac{6}{\sqrt{15\pi}} ZR^2 \beta_2 (1 + 0.36\beta_2) \cos(\gamma + 30^\circ), \quad (7)$$

under the assumption of a uniform charge distribution. The value of  $\gamma$  was taken to be  $-25^\circ$  [1]. The quadrupole moments and deformations calculated in this work are given in Table VII.

The quadrupole moments calculated here have been compared with the ground-state deformation predicted by Möller and Bengtsson [1], incorporating triaxial degrees of freedom. With a predicted ground-state deformation of  $\beta_2 = 0.20$  and  $\gamma = -25^\circ$ , the rigid-rotor rotational model calculates a quadrupole moment of  $Q_t = 4.9 e \text{ b}$ . To reproduce this theoretical value from the experimental lifetime measurement of the  $6^+$  to  $4^+$  transition in Band 1, all possible

TABLE VII. Electromagnetic properties of the low-lying states in Bands 1 and 2 of  $^{144}\text{Dy}$  extracted from the calculated lifetime measurements.

Band	$E_\gamma$ (keV)	$I_i^\pi$	$\tau$ (ps)	$B(E2)$ (W.u.)	$ Q_t $ ( $e \text{ b}$ )	$ \beta_2 $
1	752	$6^+$	3.5(7)	21.6(43)	1.8(3)	0.056(6)
1	649	$8^+$	2.1(5)	75(17)	3.2(3)	0.12(1)
1	610	$10^+$	2.8(7)	77(19)	3.2(4)	0.12(1)
1	665	$12^+$	0.72(38)	208(111)	5.1(14)	0.19(3)
2	552	$10^+$	11.5(23)	31(6)	2.03(21)	0.077(4)

Clebsch-Gordan coefficients available for this transition were compared. The Clebsch-Gordan coefficient that most closely resembled the Möller and Bengtsson theoretical calculation required the maximum value of  $K = 4\hbar$  for the angular momentum projection onto the symmetry axis. This result gives a value of  $Q_t = 3.93 e \text{ b}$ , corresponding to a deformation of  $\beta_2 = 0.15$ . This is lower than the value quoted by Möller and Bengtsson and suggests one of two possibilities: Either the angular momentum projection onto the symmetry axis is no longer a good quantum number and cannot be used to determine quadrupole moments in a triaxial regime or the ground-state triaxiality may be lost at low rotations, as nucleons begin to align, and the nucleus takes on an axially symmetric shape. To fully investigate this, lifetime measurements are required for the  $2^+$  and  $4^+$  excited states, in conjunction with further theoretical study to assess the possible loss of the angular momentum projection  $K$  as a good quantum number within a triaxial regime.

It should be noted, however, that it is still possible to infer nuclear properties from the observed trend in the deformations measured for states in Band 1. The nuclear shape is observed to increase in deformation as the nuclear spin increases, without any sudden changes. This is unexpected for transitions across an observed backbend, where the deformation may be expected to significantly reduce as single particles are aligned. This may be a consequence of the loss of the ground-state triaxiality as nucleons begin to align at low spin. In this scheme, it is possible that the nucleus takes on a more prolate deformation, in line with the assignment of the excited  $10^+$  state in Band 1 to the  $\pi(\text{FG})$  configuration, whose aligned F and G quasiprotons along the rotation axis are expected to be prolate driving. Such a scenario would also provide a possible explanation for the long-lived two-quasineutron state decaying into the ground-state sequence from Band 3, as the high- $\Omega$ ,  $h_{11/2}$  neutron states that make up this configuration are expected to be oblate driving (see later).

Recent work on  $^{142}\text{Gd}$  suggests that the excitations above the three coexisting  $10^+$  states can be described by rotation around one of the three principal axes of a triaxially deformed nuclear shape [7]. However, it has also been suggested by Starzecki *et al.* [5], in the study of  $^{140}\text{Sm}$ , that the nucleus may take on the properties of rotating prolate and oblate shapes in the different bands above the first crossings, where the apparent ground-state triaxiality is lost once nucleons start to align. This

TABLE VIII. Lifetimes of the excited two-quasiproton and two-quasineutron  $10^+$  states in the lower mass even-even isotones and their theoretical ground-state (G.S.) deformations [1]. Data not from the current experiment were taken from Refs. [5,11]. Where no value is given, the state has not been observed. The quoted energies correspond to those of the  $\gamma$  rays depopulating the states.

Nucleus	Two-quasiproton $10^+$ state		Two-quasineutron $10^+$ state		G.S. deformation [1]		
	$E_\gamma$ (keV)	$\tau$ (ns)	$E_\gamma$ (keV)	$\tau$ (ns)	$\beta_2$	$\beta_4$	$\gamma$
$^{144}_{66}\text{Dy}$	552	0.012(2)	528	$0.010 < \tau \lesssim 16$	0.20	0.04	$-25^\circ$
$^{142}_{64}\text{Gd}$	407	0.53(7)	379	4.9(4)	0.175	0.04	$-30^\circ$
$^{140}_{62}\text{Sm}$	241	8.9(12)	202	32.2(26)	0.175	0.04	$-30^\circ$
$^{138}_{60}\text{Nd}$	–	–	67	592(72)	0.15	0.04	$-30^\circ$
$^{136}_{58}\text{Ce}$	–	–	106	3174(577)	0.15	0.02	$-27.5^\circ$

description would account for several of the features observed within and between these bands. First, the Nilsson orbitals assigned to the observed alignments favor both prolate and oblate deformations for the proton and neutron crossings, in Bands 1 and 2 and in Band 3, respectively. Second, Band 3 appears to have no links with either Bands 1 or 2, which, themselves, are linked via several weak interband transitions. This would suggest that the structure or deformation of Band 3 may differ from that of the two bands built upon quasiproton configurations. Third, the lifetimes of the three bandheads appear to differ quite drastically. Previous lifetime measurements in  $^{142}\text{Gd}$  [5] and  $^{140}\text{Sm}$  [5] show that the analogous states in these nuclei are isomeric, with lifetimes of the order of several nanoseconds. Table VIII compares the lifetime estimates for the  $10^+$  states in Bands 2 and 3 of  $^{144}\text{Dy}$  with those of the neighboring nuclei.

Although the lifetime of the two-quasiproton  $10^+$  state measured in this work is reasonably small, the state built upon the two-quasineutron excitation in Band 3 shows a possible large value, lying outside of the range within which this RDDS experiment was sensitive. An approximate upper limit of 16 ns has been assigned to the two-quasineutron  $10^+$  state, based upon the velocity with which the observed nuclei recoiled out of the focus of the JUROGAM array (see Sec. III B). The trend of decreasing lifetimes as proton number increases, from the lower mass even-even isotones to  $^{144}\text{Dy}$ , suggest that 16 ns is an appropriate upper limit. The alignment plots in Fig. 11 show that the ground-state band is already aligning at  $6\hbar$ , which may imply that the hindrance observed in these long-lived  $10^+$  states most likely does not result from any large reorganization of the nuclear spin with respect to the nuclear symmetry axis ( $K$ -isomerism). Instead, these long lifetimes are assumed to arise from a change in the nuclear shape, with the difference between the observed lifetimes attributed to the different change in shape above the crossings. Shape isomers are established where several minima are present in potential energy surface calculations with different deformations. Transitions between these stable states are thus hindered, resulting in longer than expected nuclear lifetimes. In this work on  $^{144}\text{Dy}$ , it may be expected that the transition between the different shapes and deformations above the two  $10^+$  states in Bands 2 and 3 and the ground state triaxial shape

is hindered by some reconfiguration of the nuclear spin with respect to the entire volume of the nucleus. The lack of any long-lived component in the decay of the  $10^+$  state in Band 1 suggests that this shape change is less drastic in this band than in the other two bands, pointing toward a prolate-shape polarization of Band 1 below the crossing.

The decreasing trend in lifetimes of the two  $10^+$  states in Bands 2 and 3, with increasing proton number  $Z$ , can be clearly seen in Table VIII. The lifetimes of the states appear to decrease, to the extent where, in  $^{144}\text{Dy}$ , the two-quasiproton state is no longer isomeric. In the case of  $^{138}\text{Nd}$  [9] and  $^{136}\text{Ce}$  [10], only the excited neutron states have been observed. This may result from the fact that, in each instance, the two-quasiproton  $10^+$  states have been attributed to excitations in the  $h_{11/2}$  shell. The neighboring even-odd nucleus  $^{137}\text{Pr}$  [40] has a ground state spin of  $J^\pi = 5/2^+$ , implying that the single proton at the Fermi surface lies lower in energy than the  $h_{11/2}$  orbitals. For the neighboring even-even nuclei  $^{138}\text{Nd}$  and  $^{136}\text{Ce}$ , this would suggest that the low-lying  $\pi(h_{11/2})$  crossing is not observed, as it would require a large amount of energy to promote protons into these orbitals high above the Fermi surface. The change in lifetimes between the  $N = 78$  isotones is then likely to arise from the change in nuclear shape, as the occupancy of low-lying  $\pi(h_{11/2})$ , prolate-driving orbitals increases. The filling of these proton  $h_{11/2}$  states drives the nucleus toward a more prolate deformation below the first crossing and may result in a possible reduction in the observed triaxiality of the ground-state configuration (see Table VIII). In turn, this may reduce the amount of energy required to rotate the nucleus to the point where aligning nucleons at the Fermi surface, and forming more prolate and oblate structures, becomes favorable. Indeed, the excitation energy of the excited  $10^+$  states in  $^{144}\text{Dy}$  is lower than in  $^{142}\text{Gd}$ , which lie lower than those observed in  $^{140}\text{Sm}$ . In this instance, the change in nuclear shape may be seen to become less drastic above the crossings and  $10^+$  states, the result of which could produce a decay lifetime from the bandheads that may resemble those of rotational states more than single-particle transitions between different shapes. Further lifetime measurements and theoretical calculations including triaxiality, such as TRS plots, would be useful to fully explore this effect in this region.

## V. CONCLUSION

In summary, the JUROGAM  $\gamma$ -ray spectrometer and Köln differential-plunger device, coupled to the RITU gas-filled recoil separator and GREAT focal-plane spectrometer, has allowed the study of both the spectroscopic and lifetime properties of known and new states in  $^{144}\text{Dy}$ . The nuclear structure has been extended and reorganized based upon consideration of neighboring nuclei as well as lifetime measurements. This experiment has resulted in the observation of three bands built upon two-quasiparticle excitations, for which CSM calculations and the examination of alignment, Routhian, and energies minus a rigid-rotor reference plots allowed single-particle configurations to be assigned. The presence of a known dipole band at moderate spin has been confirmed and four new dipole bands have been established in this work. Measurements of  $g_k$  from  $\gamma$ -ray branching ratios have helped confirm the nature of DB3 in terms of its magnetic rotation, and the observed trend in  $B(M1)/B(E2)$  branching ratios has shed light on the possible competing effects of rotationally driven excitations. Lifetime data have been analyzed for the two  $10^+$  states in Bands 2 and 3. The results appear to show a continuation in the trend of decreasing lifetimes seen in the lower mass even-even isotones, which has been attributed to the deformation driving effects of protons in low- $\Omega$   $h_{11/2}$  intruder orbitals. Lifetime measurements across the first alignment in Band 1 appear to show a continuation

of the ground-state deformation, even though energies minus a rigid-rotor reference data show this structure to be no longer yrast, and arising from an unfavored crossing. It has been postulated that above the first crossing  $^{144}\text{Dy}$  exhibits a possible shape coexistence or triaxial rotation. The behavior of the nuclear structure above these crossings appears to favor a shape coexistence with Bands 1 and 2 favoring a prolate deformation and Band 3 an oblate one. However, further study and theoretical calculations including triaxiality, as well as lifetime measurements with different regions of sensitivity, are required to fully investigate this phenomena in more detail.

## ACKNOWLEDGMENTS

Useful discussions with T. Grahn are gratefully acknowledged. This work has been supported by the EU 6th Framework Programme, “Integrating Infrastructure Initiative Transnational Access,” Contract No. 506065 (EURONS), and by the Academy of Finland under the Finnish Centre of Excellence Programme 2006–2011 (Nuclear and Accelerator Based Physics Programme at JYFL). The authors acknowledge the support of the EPSRC/IN2P3 LOANPOOL and GAMMAPOOL for the loan of the JUROGAM detectors. M.G.P acknowledges support by the STFC. D.M.C. acknowledges the support of the STFC through Contract No. PP/F000855/1. C.S and P.T.G. acknowledge the support of the Academy of Finland through Contract Nos. 209430 and 119290, respectively.

- 
- [1] P. Möller *et al.*, *At. Data Nucl. Data Tables* **94**, 758 (2008).
  - [2] R. Lieder *et al.*, *Eur. Phys. J. A* **13**, 297 (2002).
  - [3] A. Pasternak *et al.*, *Eur. Phys. J. A* **23**, 191 (2005).
  - [4] E. Lieder *et al.*, *Eur. Phys. J. A* **35**, 135 (2002).
  - [5] W. Starzecki *et al.*, *Phys. Lett. B* **200**, 419 (1988).
  - [6] D. Bazzacco *et al.*, *Phys. Lett. B* **206**, 404 (1988).
  - [7] B. G. Carlsson, I. Ragnarsson, R. Bengtsson, E. O. Lieder, R. M. Lieder, and A. A. Pasternak, *Phys. Rev. C* **78**, 034316 (2008).
  - [8] D. Bazzacco *et al.*, Annual report 1987, No. LNL-INFN (REP)-014/88, p. 7 (1988).
  - [9] M. Müller-Veggian *et al.*, *Nucl. Phys. A* **344**, 89 (1980).
  - [10] M. Müller-Veggian *et al.*, *Nucl. Phys. A* **304**, 1 (1978).
  - [11] N. Yoshikawa, *Nucl. Phys. A* **243**, 143 (1975).
  - [12] M. Sugawara *et al.*, *Phys. Rev. C* **79**, 064321 (2009).
  - [13] P. J. R. Mason *et al.*, *Phys. Lett. B* **683**, 17 (2010).
  - [14] P. J. R. Mason *et al.*, *Phys. Rev. C* **81**, 024302 (2010).
  - [15] R. D. Page *et al.*, *Nucl. Instrum. Methods Phys. Res. B* **204**, 634 (2003).
  - [16] M. Leino *et al.*, *Nucl. Instrum. Methods Phys. Res. B* **99**, 653 (1995).
  - [17] M. Leino, *Nucl. Instrum. Methods Phys. Res. B* **126**, 320 (1997).
  - [18] L. Cleemann *et al.*, *Nucl. Instrum. Methods* **156**, 477 (1978).
  - [19] P. T. Greenlees *et al.*, *AIP Conf. Proc.* **764**, 237 (2005).
  - [20] P. T. Greenlees *et al.*, *Eur. Phys. J. A* **25**, 599 (2005).
  - [21] I. Lazarus *et al.*, *IEEE Trans. Nucl. Sci.* **48**, 567 (2001).
  - [22] P. Rahkila, *Nucl. Instrum. Methods Phys. Res. A* **595**, 637 (2008).
  - [23] W. T. Milner (private communication).
  - [24] D. C. Radford, *Nucl. Instrum. Methods Phys. Res. A* **361**, 297 (1995).
  - [25] A. Dewald, S. Harissopulos, and P. von Brentano, *Z. Phys. A* **334**, 163 (1989).
  - [26] G. Böhm, A. Dewald, P. Petkov, and P. von Brentano, *Nucl. Instrum. Methods* **329**, 248 (1993).
  - [27] O. Möller *et al.*, *Phys. Rev. C* **74**, 024313 (2006).
  - [28] A. Dewald *et al.*, *Phys. Rev. C* **68**, 034314 (2003).
  - [29] L. Goettig *et al.*, *Nucl. Phys. A* **464**, 159 (1987).
  - [30] F. R. Espinoza-Quiñones *et al.*, *Phys. Rev. C* **60**, 054304 (1999).
  - [31] H. Emling *et al.*, *Nucl. Phys. A* **419**, 187 (1984).
  - [32] R. C. Pardo, S. Gales, R. M. Ronningen, and L. H. Harwood, *Phys. Lett. B* **91**, 41 (1980).
  - [33] R. Bengtsson and S. Frauendorf, *Nucl. Phys. A* **314**, 27 (1979).
  - [34] S. M. Harris, *Phys. Rev.* **138**, B509 (1965).
  - [35] M. Sferrazza *et al.*, *Z. Phys. A* **350**, 5 (1994).
  - [36] H. Roth *et al.*, *Eur. Phys. J. A* **10**, 275 (2001).
  - [37] R. M. Clark, *J. Phys. G* **25**, 695 (1999).
  - [38] S. Frauendorf, *Rev. Mod. Phys.* **73**, 463 (2001).
  - [39] T. Kibdi *et al.*, *Nucl. Instrum. Methods Phys. Res. A* **589**, 202 (2008).
  - [40] E. Dragulescu *et al.*, *Nucl. Phys. A* **548**, 435 (1992).